

Flexoelectricity and surface ferroelectricity in water ice

Authors: X. Wen^{1,3}, Q. Ma¹, A. Mannino^{4,5}, M. Fernandez-Serra^{4,5}, S. Shen^{1*}, G. Catalan^{2,3*}

Affiliations:

¹State Key Laboratory for Strength and Vibration of Mechanical Structures, School of Aerospace Engineering, Xi'an Jiaotong University, Xi'an, China.

²ICREA—Institutio Catalana de Recerca i Estudis Avançats, Passeig Lluís Companys 23, Barcelona, Catalonia

³Institut Catala de Nanociencia i Nanotecnologia (ICN2), CSIC and The Barcelona Institute of Nanoscience and Technology (BIST), Campus Universitat Autònoma de Barcelona, Bellaterra, Catalonia.

⁴Physics and Astronomy Department, Stony Brook University, Stony Brook, New York 11794-3800, United States

⁵Institute for Advanced Computational Science, Stony Brook University, Stony Brook, New York 11794-3800, United States

*Corresponding author. Email: sshen@mail.xjtu.edu.cn; gustau.catalan@icn2.cat

Abstract:

The phase diagram of ice is complex and contains many phases, but the most common (frozen water at ambient pressure, also known as Ih ice) is a non-polar material despite individual water molecules being polar^{1,2}. Consequently, ice is not piezoelectric and cannot generate electricity under pressure³. On the other hand, it can in theory be flexoelectric because the coupling between polarization and strain gradient is universal^{4,5}. Therefore, ice may polarize under bending or any inhomogeneous deformation. Here we report the flexoelectricity of ice, and show that it can account for important ice-electrification processes occurring in nature, such as the genesis of lightning in storm clouds. In addition, the sensitivity of flexoelectricity to surface boundary conditions has revealed the presence of a ferroelectric phase that appears around 163 K confined within the surface “skin layer” of bulk ice.

Main Text:

Ice, formed by hydrogen bonding of water molecules (H_2O), is one of the most widespread and abundant solids on earth. Manifesting as snowflakes, frosts, and glaciers in nature, ice plays an essential role in geology, meteorology, and astronomy¹. Moreover, even liquid water is ice-like when nano-confined or at the interface with solids⁶, which renders the physics of ice also relevant to life science and electrochemistry^{7,8}. Despite the ongoing interest and large body of knowledge on ice³, new phases^{9,10} and anomalous properties¹¹ continue to be discovered, suggesting our understanding of this ubiquitous material is far from complete.

An interesting open question concerns the electromechanical properties of ice. Despite the polarity of individual water molecules, common ice Ih is not piezoelectric³, which precludes electromechanical transducer applications. The lack of piezoelectricity in ordinary ice Ih is due to the geometric frustration introduced by the so-called Bernal-Fowler rules^{1,3}: two hydrogen protons must be adjacent to each oxygen atom, but there can only be one hydrogen proton between two oxygen atoms. As a result, in contrast to the oxygen atoms, which are arranged in a hexagonal lattice, the hydrogen atoms do not exhibit long-range order³, resulting in randomly oriented water dipoles and thus no macroscopic piezoelectricity. Yet ice is known to generate electricity under mechanical stress in nature. For example, ice collisions and fractures cause electrifications in clouds^{12,13} and polar regions^{14,15}. The underpinning electromechanical mechanism of these natural phenomena remains elusive.

In this context, we bring our attention to flexoelectricity, a coupling between electrical polarization and strain gradients that, contrary to piezoelectricity, can exist in materials of any symmetry^{4,5}. In theory, then, it may also exist in ice. Yet, despite a growing awareness of flexoelectricity and its consequences in other materials¹⁶⁻²¹, the flexoelectricity of ice remains unknown. In this article we report its measurement and examine some of its repercussions.

We have prepared ice capacitors by freezing at ambient pressure a layer of ultrapure water (milli-Q, resistivity $>10 \text{ MOhm}\cdot\text{cm}$) between two electrodes of gold-coated aluminum (Fig. 1a and b). Our samples are polycrystalline (mean grain size $\sim 77 \text{ }\mu\text{m}$) with a preferential orientation of [001], and are at ordinary Ih phase in the experimental temperature range as verified by X-

ray diffraction and Raman spectroscopy (Supplementary Fig. S1). Piezoelectric measurements confirm the non-piezoelectric nature of the ice (Supplementary Fig. S2).

To measure ice flexoelectricity, we have used a dynamic mechanical analyzer (DMA) to deliver an oscillating three-point bending deformation to the ice capacitor (Supplementary Fig. S3 and MovieS1). The bending deformation (measured by a displacement sensor) and the bending-induced charge (collected by a charge amplifier) are synchronously recorded by an oscilloscope, and are then used to calculate strain gradients and polarization respectively. Fig. 1c plots the Fourier-filtered first-harmonic data of the applied displacement and the induced charge. The induced polarization, measured as a function of applied a.c. strain gradient, is plotted in Fig. 1d. It shows the linear dependence expected for a flexoelectric material. The slope of the linear fit (1.65 nC/m) represents the effective flexoelectric coefficient μ_{13}^{eff} of ice Ih. The results shown in Fig. 1c and d were obtained at 237 K, a temperature well below melting, and around which ice flexoelectricity was found to be relatively temperature-independent and far from any phase transition anomaly, as we show next.

The temperature dependence of flexoelectricity was measured in the range between 143 K and 273 K simultaneously with the mechanical response of the ice slabs. Representative results for three samples are plotted in Fig. 2a. Three distinct regimes can be identified. Above 248 K, flexoelectricity starts to increase and the phase angle between strain gradient and induced polarization charge shifts away from 0 deg (Fig. 2a and b), which are also accompanied by the onset of mechanical creep (Fig. 2c). These anomalies coincide with the ice surface transition to quasi-liquid layers (QLL) in order to reduce the free energy²²⁻²⁵, with a wide critical temperature range from 213 K to 253 K²⁶⁻³⁰ (see Supplementary Fig. S4 for direct comparison between reported QLL results and our measurements). The QLL of ice is known to facilitate charge transport²⁴ and grain-boundary sliding³¹, consistent with the softening of our samples above 248 K (Fig 2c). On the other hand, free charge motion can increase the magnitude of flexoelectricity¹⁷ and shift its phase angle³², as observed in Fig 2a and 2b. The results therefore indicate that the flexoelectric and mechanical anomalies above 248 K are affected by QLL. To ensure a creep-free initial condition, measurements were started from about 223 K (i.e. below

the QLL temperature) rather than 273 K, then cooled down to 143 K (Supplementary Fig. S5), finally followed by heating measurements all the way up to 273 K (Fig. 2 and Fig. 3).

In the temperature range between 203 K to 248 K, the flexoelectric coefficient was found to be quite constant around 1~3 nC/m. As a reference for comparison, this is in the same range as dielectric ceramics such as SrTiO₃³³, TiO₂¹⁷, or PbZrO₃³⁴. Since flexoelectricity is directly proportional to dielectric permittivity^{4,5}, this result is consistent with the relatively high dielectric constant of bulk ice, $\epsilon_r \sim 100$ ³. The flexocoupling coefficient (flexoelectric constant divided by dielectric permittivity) is ~2.3 volts, which agrees with the 1-10V expected range for intrinsic flexoelectricity in solids⁵. This, together with the stable behavior as a function of temperature, suggests that 2 ± 1 nC/m is the intrinsic value of the flexoelectric coefficient of ice. Below 203 K, however, the flexoelectric coefficient begins to grow again, reaching a peak value of ~7.6 nC/m at around 163 K (± 5 K) (Fig. 2a). Such a temperature dependence of flexoelectricity has been observed before in ceramic materials with ferroelectric or antiferroelectric phase transitions³⁴⁻³⁶, so a question emerges: is the flexoelectric anomaly of ice related to a ferroelectric phase transition?

Ferroelectric ice exists. Doping bulk ice with alkali hydroxides can cause proton rearrangement and transform ice-Ih to ferroelectric ice-XI at 72 K¹. However, the apparent Curie temperature of our ice slabs is ~100 K higher than in bulk doped ice, and the phase diagram of ambient-pressure ice does not contain any phase transition between 72 K and the melting temperature^{1,2}. Moreover, the mechanical response of our samples (Fig. 2c) shows no sign of any structural phase transition, nor do the Raman measurements as a function of temperature of our samples show any change of symmetry (Supplementary Fig. S1). It is therefore hard to attribute the flexoelectric peak at ~163 K to a bulk ferroelectric transition. Moreover, the maximum bending-induced stress in the surfaces of our sample is ~0.005Gpa (Supplementary Fig. S6), two orders of magnitude smaller than the minimum stress that can cause a phase transition in ice³⁷⁻³⁹. On the other hand, ultra-thin films of ice grown on platinum substrates have been reported to become ferroelectric^{40,41} around 163 K~175 K^{41,42}. Our slabs are thick (~2 mm) and with gold electrodes, but the similarity between our flexoelectric peak temperature and the reported Curie temperature of thin films is tantalizing.

A unique feature of flexoelectricity is that it contains comparable contributions from the bulk and the surface, irrespective of the sample thickness^{43,44}; even in thick samples, surfaces can still determine the sign and magnitude of the effective flexoelectric coefficient^{17,32,45,46}. Given the inherently important contribution of surfaces to total flexoelectricity, the lack of evidence for a bulk phase transition, and the existence of ferroelectricity in thin films, we hypothesize that the origin of the flexoelectric peak is a ferroelectric phase transition confined within the surface of our samples. In a slab with opposite polar surfaces, surface piezoelectricity can contribute to effective flexoelectricity as depicted in Fig. 3a: under bending, the different signs of the strain (compressive on one side, tensile on the other) cause a difference in polarization, which is additional to the bulk flexoelectricity. Skin layers with distinct properties are not uncommon in oxide electroceramics^{47,48}, so their existence in H₂O would not be unreasonable.

If the ferroelectric polarization is confined to the surface, we expect it to be sensitive to interfacial boundary conditions such as the electrode material. We have therefore modified our ice-capacitor interfaces by replacing the Au electrodes with other metals. Measurements on three different Pt/ice/Pt capacitors are presented in Fig. 3b, showing a similar temperature dependence of flexoelectricity but a larger maximum of ~15 nC/m at ~ 158 K (± 5 K) (see Supplementary Fig. S8 for phase angle). The flexoelectric peak of ice with Pt electrodes is larger than that with Au electrodes (Fig. 3b). This result is consistent with Sugimoto's proposed explanation for the origin of ferroelectricity in thin films⁴¹, whereby interfacial ferroelectric ordering is triggered by electron transfer from the surface to the electrode in order to equilibrate chemical potentials. The work function Φ of gold (~5.1 eV)⁴⁹ is higher than that of ice (~4.4 eV)^{50,51}, and the work function of Pt (~5.65 eV)⁴⁹ is even higher, resulting in a bigger poling field and consistent with the observed higher flexoelectric peak.

Conversely, the work-function of Al (about 4.28 eV⁴⁹) is smaller than those of Au and Pt and very close to that of ice. The interfacial field between ice and Al is therefore very small, and the ice capacitors with Al electrodes show no visible flexoelectric peak (Fig. 3b). In Fig. 3c we have plotted the peak value of the flexoelectric coefficient as a function of the electrode work-functions, showing a direct proportionality. We further studied the effect of the pre-poling

field on the flexoelectric coefficient and found a classical butterfly loop (Fig. 3d), which provides further evidence for ferroelectricity. Note that flexoelectricity was measured after switching off the voltage, which eliminates the interference from leakage currents⁵². The measurement of hysteresis, a defining feature of ferroelectricity, has so far been elusive due to the difficulty of applying electrodes to ultra-thin films such as Sugimoto's or the need for impossibly high switching voltages. Besides supporting the existence of interfacial ferroelectricity, therefore, the present results also showcase how flexoelectricity can be utilized to explore surface properties while retaining the convenience of bulk measurements.

To further understand the microscopic origin of the surface phase transition, we computed the surface free energies of both proton-ordered ice XI-Au[111] and proton-disordered ice Ih-Au[111] interfaces using density functional theory. Although our samples are polycrystalline (both the ice and the electrodes), X-ray diffraction (Supplementary Fig. S1) shows that the predominant out-of-plane orientation of the ice grains is hexagonal [001], and for cubic [111] for the electrodes, as assumed in the model.

It has been previously shown, both experimentally and theoretically^{40,53-55}, that metallic Au, Pt, and Pd [111] surfaces affect the dipole orientation of H₂O at the interface. Motivated by these studies, we established two models, of which one contains the ice-XI-Au[111] interface with the ice-XI dipole pointing towards the metal surface (Fig. 4a) and the other one contains the ice-Ih-Au[111] interface without ordered dipoles (Fig. 4b). By comparing the difference in cohesive energy between these two systems and that between bulk ice XI and bulk ice Ih without the Au slab, we find that the Au interface creates an enhanced stability of the proton ordered phase by 140 meV. Taking this enhanced stability into account in the Helmholtz free energy diagram, we predict the phase transition temperature from the proton-disordered (Ih) to the proton-ordered phase (XI) can be raised from 72 K to 152 K (Fig. 4c, Supplementary S5), which is comparable to the surface phase transition at ~163 K observed in our experiments. Further details of the calculations are provided in the supplementary information.

Lastly, we examine some consequences of the ice flexoelectricity in nature. It has long been known^{12,13,24,56} that collisions between ice particles cause charge separation in clouds and eventually cause lightning. Since, as mentioned at the beginning, ice is not piezoelectric, the

mechanism whereby such mechanical collisions generate an electrical output has remained an open question. Flexoelectricity may offer some answers in this context, as strain gradients can be very large at small size scales such as those involved in nano/micro-indentations, fractures and friction^{18,19,57}.

To quantify the link between flexoelectricity and ice electrification in storm clouds, we use the Hertzian model of elastic deformations (see details in Supplementary S7) to calculate the strain gradient and multiply it by the measured flexoelectric coefficient to map the flexoelectricity induced in a typical ice-graupel collision (Fig. S5a). Fig. 5b plots the flexoelectric polarization beneath the indentation surface of the larger (descending) particle. The induced flexoelectric polarization is the largest at the interface and decays progressively away. This surface polarization creates a strong electric field (aka the depolarizing field) that must be compensated by a screening charge. Using our measured flexoelectric coefficient, adopting parameters of typical ice collisions reported in the literature (Supplementary Table S1), and integrating the vertical polarization over the contact area, our model yields a surface charge of the order of $10^0\sim 10^2$ fC per collision (Supplementary Fig. S12), which agrees with experiments^{56,58-64}. Moreover, our model can reproduce other representative features of ice-graupel electrification: size dependence, velocity dependence and the reversal of charge-transfer direction during collisions (Fig. 5c~e). Another example of natural ice electrification occurs at fractures, and the known experimental features are also excellently reproduced, both qualitatively and quantitatively, by incorporating flexoelectricity into the deformation models (see Supplementary S8, Fig. S13).

The existence of flexoelectricity in ice is not surprising, given the universality of this phenomenon. What is unexpected is what the flexoelectric measurements have revealed about surface phase transitions of ice. More important, now that an origin for the electromechanical activity of ordinary Ih ice has been identified, the consequences of flexoelectricity for the multitude of natural processes in which ice and ice-like interfacial water are involved can finally be understood.

References and Notes

- 1 Bartels-Rausch, T. *et al.* Ice structures, patterns, and processes: A view across the icefields. *Reviews of Modern Physics* **84**, 885-944, doi:10.1103/RevModPhys.84.885 (2012).
- 2 Salzmann, C. G. Advances in the experimental exploration of water's phase diagram. *The Journal of chemical physics* **150**, 060901 (2019).
- 3 Petrenko, V. F. & Whitworth, R. W. *Physics of ice*. (OUP Oxford, 1999).
- 4 Tagantsev, A. K. Piezoelectricity and Flexoelectricity in Crystalline Dielectrics. *Phys Rev B* **34**, 5883-5889, doi:DOI 10.1103/PhysRevB.34.5883 (1986).
- 5 Zubko, P., Catalan, G. & Tagantsev, A. K. Flexoelectric Effect in Solids. *Annu Rev Mater Sci* **43**, 387-421, doi:10.1146/annurev-matsci-071312-121634 (2013).
- 6 Fumagalli, L. *et al.* Anomalously low dielectric constant of confined water. *Science* **360**, 1339-1342, doi:10.1126/science.aat4191 (2018).
- 7 Ball, P. Water as an active constituent in cell biology. *Chem Rev* **108**, 74-108, doi:10.1021/cr068037a (2008).
- 8 Wang, Y.-H. *et al.* In situ Raman spectroscopy reveals the structure and dissociation of interfacial water. *Nature* **600**, 81-85 (2021).
- 9 Kapil, V. *et al.* The first-principles phase diagram of monolayer nanoconfined water. *Nature* **609**, 512-516 (2022).
- 10 Rosu-Finsen, A. *et al.* Medium-density amorphous ice. *Science* **379**, 474-478 (2023).
- 11 Xu, P. *et al.* Elastic ice microfibers. *Science* **373**, 187-192, doi:10.1126/science.abh3754 (2021).
- 12 Reynolds, S., Brook, M. & Gourley, M. F. Thunderstorm charge separation. *Journal of Atmospheric Sciences* **14**, 426-436 (1957).
- 13 Saunders, C. J. P. A. E. Charge separation mechanisms in clouds. 335-353 (2008).
- 14 Thiel, D. V. Electromagnetic emission (EME) from ice crack formation: preliminary observations. *Cold Regions Science and Technology* **21**, 49-60, doi:10.1016/0165-232x(92)90005-f (1992).
- 15 Fifolt, D. A., Petrenko, V. F. & Schulson, E. M. Preliminary study of electromagnetic emissions from cracks in ice. *Philosophical Magazine B* **67**, 289-299, doi:10.1080/13642819308220133 (1993).
- 16 Lu, H. *et al.* Mechanical writing of ferroelectric polarization. *Science* **336**, 59-61, doi:10.1126/science.1218693 (2012).
- 17 Narvaez, J., Vasquez-Sancho, F. & Catalan, G. Enhanced flexoelectric-like response in oxide semiconductors. *Nature* **538**, 219-221, doi:10.1038/nature19761 (2016).
- 18 Yang, M. M., Kim, D. J. & Alexe, M. Flexo-photovoltaic effect. *Science* **360**, 904-907, doi:10.1126/science.aan3256 (2018).
- 19 Vasquez-Sancho, F., Abdollahi, A., Damjanovic, D. & Catalan, G. Flexoelectricity in bones. *Adv Mater* **30**, 1705316, doi:10.1002/adma.201705316 (2018).
- 20 Shu, L. *et al.* Photoflexoelectric effect in halide perovskites. *Nat Mater* **19**, 605-609, doi:10.1038/s41563-020-0659-y (2020).
- 21 Torbati, M., Mozaffari, K., Liu, L. & Sharma, P. Coupling of mechanical deformation and electromagnetic fields in biological cells. *Rev Mod Phys* **94**, 025003 (2022).

- 22 Faraday, M. On certain conditions of freezing water. *Journal of the Franklin Institute, of the State of Pennsylvania, for the Promotion of the Mechanic Arts; Devoted to Mechanical and Physical Science, Civil Engineering, the Arts and Manufactures, and the Recording of American and Other Patent Inventions (1828-1851)* **20**, 283 (1850).
- 23 Fletcher, N. H. Surface structure of water and ice. *Philosophical Magazine* **7**, 255-269 (1962).
- 24 Dash, J. G., Rempel, A. W. & Wettlaufer, J. S. The physics of premelted ice and its geophysical consequences. *Reviews of Modern Physics* **78**, 695-741, doi:10.1103/RevModPhys.78.695 (2006).
- 25 Slater, B. & Michaelides, A. Surface premelting of water ice. *Nature Reviews Chemistry* **3**, 172-188, doi:10.1038/s41570-019-0080-8 (2019).
- 26 Golecki, I. & Jaccard, C. Intrinsic surface disorder in ice near the melting point. *Journal of Physics C: Solid state physics* **11**, 4229 (1978).
- 27 Dosch, H., Lied, A. & Bilgram, J. Glancing-angle X-ray scattering studies of the premelting of ice surfaces. *Surface science* **327**, 145-164 (1995).
- 28 Döppenschmidt, A. & Butt, H.-J. Measuring the thickness of the liquid-like layer on ice surfaces with atomic force microscopy. *Langmuir* **16**, 6709-6714 (2000).
- 29 Bluhm, H., Ogletree, D. F., Fadley, C. S., Hussain, Z. & Salmeron, M. The premelting of ice studied with photoelectron spectroscopy. *Journal of Physics: Condensed Matter* **14**, L227 (2002).
- 30 Sadtchenko, V. & Ewing, G. E. A new approach to the study of interfacial melting of ice: infrared spectroscopy. *Canadian journal of physics* **81**, 333-341 (2003).
- 31 Ribeiro, I. d. A. & Koning, M. d. Grain-boundary sliding in ice Ih: Tribology and rheology at the nanoscale. *The Journal of Physical Chemistry C* **125**, 627-634 (2021).
- 32 Ma, Q., Wen, X., Lv, L., Deng, Q. & Shen, S. On the flexoelectric-like effect of Nb-doped SrTiO₃ single crystals. *Applied Physics Letters* **123** (2023).
- 33 Zubko, P., Catalan, G., Buckley, A., Welche, P. R. & Scott, J. F. Strain-gradient-induced polarization in SrTiO₃ single crystals. *Phys Rev Lett* **99**, 167601, doi:10.1103/PhysRevLett.99.167601 (2007).
- 34 Vales-Castro, P. *et al.* Flexoelectricity in antiferroelectrics. *Appl Phys Lett* **113**, doi:10.1063/1.5044724 (2018).
- 35 Ma, W. & Cross, L. E. Flexoelectricity of barium titanate. *Appl Phys Lett* **88**, 232902, doi:10.1063/1.2211309 (2006).
- 36 Narvaez, J. & Catalan, G. Origin of the enhanced flexoelectricity of relaxor ferroelectrics. *Appl Phys Lett* **104**, doi:10.1063/1.4871686 (2014).
- 37 Mishima, O., Calvert, L. & Whalley, E. 'Melting ice' I at 77 K and 10 kbar: A new method of making amorphous solids. *Nature* **310**, 393-395 (1984).
- 38 Garg, A. K. High-pressure Raman spectroscopic study of the ice Ih → ice IX phase transition. *Physica Status Solidi (a)* **110**, 467-480, doi:10.1002/pssa.2211100219 (1988).
- 39 Bartels-Rausch, T. *et al.* Ice structures, patterns, and processes: A view across the icefields. *Reviews of Modern Physics* **84**, 885 (2012).

- 40 Su, X. C., Lianos, L., Shen, Y. R. & Somorjai, G. A. Surface-induced ferroelectric ice on Pt(111). *Phys Rev Lett* **80**, 1533-1536, doi:DOI 10.1103/PhysRevLett.80.1533 (1998).
- 41 Sugimoto, T., Aiga, N., Otsuki, Y., Watanabe, K. & Matsumoto, Y. Emergent high-T_c ferroelectric ordering of strongly correlated and frustrated protons in a heteroepitaxial ice film. *Nature Physics* **12**, 1063-1068, doi:10.1038/nphys3820 (2016).
- 42 Aiga, N., Sugimoto, T., Otsuki, Y., Watanabe, K. & Matsumoto, Y. Origins of emergent high-T_c ferroelectric ordering in heteroepitaxial ice films: Sum-frequency generation vibrational spectroscopy of H₂O and D₂O ice films on Pt(111). *Physical Review B* **97**, doi:10.1103/PhysRevB.97.075410 (2018).
- 43 Shen, S. & Hu, S. A theory of flexoelectricity with surface effect for elastic dielectrics. *J Mech Phys Solids* **58**, 665-677, doi:10.1016/j.jmps.2010.03.001 (2010).
- 44 Tagantsev, A. K. & Yurkov, A. S. Flexoelectric effect in finite samples. *J Appl Phys* **112**, 044103, doi:10.1063/1.4745037 (2012).
- 45 Stengel, M. Surface control of flexoelectricity. *Phys Rev B* **90**, 201112, doi:10.1103/PhysRevB.90.201112 (2014).
- 46 Narvaez, J., Saremi, S., Hong, J., Stengel, M. & Catalan, G. Large flexoelectric anisotropy in paraelectric barium titanate. *Phys Rev Lett* **115**, 037601, doi:10.1103/PhysRevLett.115.037601 (2015).
- 47 Martí, X. *et al.* Skin layer of BiFeO₃ single crystals. *Phys Rev Lett* **106**, 236101 (2011).
- 48 Zhang, X. *et al.* Large Flexoelectriclike Response from the Spontaneously Polarized Surfaces in Ferroelectric Ceramics. *Phys Rev Lett* **121**, 057602, doi:10.1103/PhysRevLett.121.057602 (2018).
- 49 Michaelson, H. B. The work function of the elements and its periodicity. *J Appl Phys* **48**, 4729-4733, doi:10.1063/1.323539 (1977).
- 50 Buser, O. & Aufdermaur, A. in *Electrical processes in atmospheres* 294-301 (Springer, 1976).
- 51 Mazzega, E., del Pennino, U., Loria, A. & Mantovani, S. Volta effect and liquidlike layer at the ice surface. *The Journal of Chemical Physics* **64**, 1028-1031 (1976).
- 52 Scott, J. F. Ferroelectrics go bananas. *Journal of Physics: Condensed Matter* **20**, doi:10.1088/0953-8984/20/02/021001 (2008).
- 53 Pedroza, L. S., Poissier, A. & Fernandez-Serra, M. V. Local order of liquid water at metallic electrode surfaces. *J Chem Phys* **142**, 034706, doi:10.1063/1.4905493 (2015).
- 54 Sugimoto, T. & Matsumoto, Y. Orientational ordering in heteroepitaxial water ice on metal surfaces. *Phys Chem Chem Phys* **22**, 16453-16466, doi:10.1039/d0cp01763a (2020).
- 55 Poissier, A., Ganeshan, S. & Fernandez-Serra, M. The role of hydrogen bonding in water-metal interactions. *Physical Chemistry Chemical Physics* **13**, 3375-3384 (2011).
- 56 Takahashi, T. Riming electrification as a charge generation mechanism in thunderstorms. *Journal of Atmospheric Sciences* **35**, 1536-1548 (1978).

- 57 Mizzi, C. A., Lin, A. Y. W. & Marks, L. D. Does flexoelectricity drive triboelectricity? *Phys Rev Lett* **123**, 116103, doi:10.1103/PhysRevLett.123.116103 (2019).
- 58 Gaskell, W. & Illingworth, A. Charge transfer accompanying individual collisions between ice particles and its role in thunderstorm electrification. *Quarterly Journal of the Royal Meteorological Society* **106**, 841-854 (1980).
- 59 Jayaratne, E., Saunders, C. & Hallett, J. Laboratory studies of the charging of soft-hail during ice crystal interactions. *Quarterly Journal of the Royal Meteorological Society* **109**, 609-630 (1983).
- 60 Caranti, G., Avila, E. & Ré, M. Charge transfer during individual collisions in ice growing from vapor deposition. *Journal of Geophysical Research: Atmospheres* **96**, 15365-15375 (1991).
- 61 Avila, E. E. & Caranti, G. M. A laboratory study of static charging by fracture in ice growing by riming. *Journal of Geophysical Research: Atmospheres* **99**, 10611-10620 (1994).
- 62 Avila, E. E., Varela, G. G. A. & Caranti, G. M. Temperature dependence of static charging in ice growing by riming. *Journal of Atmospheric Sciences* **52**, 4515-4522 (1995).
- 63 Luque, M. Y., Nollas, F., Pereyra, R. G., Bürgesser, R. E. & Ávila, E. E. Charge separation in collisions between ice crystals and a spherical simulated graupel of centimeter size. *Journal of Geophysical Research: Atmospheres* **125**, e2019JD030941 (2020).
- 64 Pereyra, R. G. & Avila, E. E. Charge transfer measurements during single ice crystal collisions with a target growing by riming. *Journal of Geophysical Research: Atmospheres* **107**, AAC 23-21-AAC 23-29 (2002).
- 65 Ordejón, P., Artacho, E. & Soler, J. M. Self-consistent order-N density-functional calculations for very large systems. *Physical review B* **53**, R10441 (1996).
- 66 Soler, J. M. *et al.* The SIESTA method for ab initio order-N materials simulation. *Journal of Physics: Condensed Matter* **14**, 2745 (2002).
- 67 Perdew, J. P., Burke, K. & Ernzerhof, M. Generalized gradient approximation made simple. *Phys Rev Lett* **77**, 3865 (1996).
- 68 Dion, M., Rydberg, H., Schröder, E., Langreth, D. C. & Lundqvist, B. I. Van der Waals density functional for general geometries. *Phys Rev Lett* **92**, 246401 (2004).
- 69 Wang, J., Román-Pérez, G., Soler, J. M., Artacho, E. & Fernández-Serra, M.-V. Density, structure, and dynamics of water: The effect of van der Waals interactions. *The Journal of chemical physics* **134** (2011).
- 70 Pamuk, B. *et al.* Anomalous nuclear quantum effects in ice. *Phys Rev Lett* **108**, 193003 (2012).
- 71 Pamuk, B., Allen, P. B. & Fernández-Serra, M. V. Electronic and nuclear quantum effects on the ice XI/ice Ih phase transition. *Physical Review B* **92**, doi:10.1103/PhysRevB.92.134105 (2015).
- 72 Heymsfield, A. J. Cloud Physics. (2003).

Methods

Preparation of electrodes. Aluminum foils with a thickness of 15 μm (BS-QT-027, Biosharp) were cut into strips with a length of 100mm and width of 5 mm, which were then chemically cleaned by acetone, ethanol, and ultrapure water sequentially. To study the electrode dependence of ice flexoelectricity, we coated a gold or platinum layer of ~ 100 nm on the surface of cleaned Al foils with an Ion Sputter Coater (MC1000, HITACHI). Copper wires were attached to the foils by a drop of silver paste (948-06G, HumiSeal), which was then solidified at 373 K for half-hour. To check the conductivity of the adhesion, we used a multimeter to measure the resistance from the copper wire to the aluminum foil. When the resistance is less than 1 Ohm, the electrodes were used for the following steps.

Preparation of water and ice capacitors. Ultrapure water produced by a water purification system (Sistema Milli-Q Advantage A10) was used as the mother material for fabricating pure ice. Water was degassed in a vacuum drying oven (DZF-6050, ShanghaiYiheng) at room temperature until no air bubbles were generated. Two pieces of cleaned aluminum foil (or sputtered with Au or Pt) were placed horizontally on the dynamic mechanical analyzer with a vertical air gap. The air gap was engineered by placing two ceramic bars on the left and right sides of the clamps as shown in Fig. 1a. Degassed ultrapure water was then added into the air gap between foils by a plastic dropper. Thanks to the surface tension, the water could maintain a good shape instead of spreading to the left and right sides. With two electrodes and one layer of water in between, a water capacitor was obtained (Fig. 1a). Then, the water capacitor was frozen at 253 K for an hour and a half to obtain the ice capacitor. By cutting the redundant electrodes on left and right sides, we had an ice capacitor ready for flexoelectric characterizations (Fig. 1b). The thickness of the ice capacitors was measured by a vernier caliper in the temperature box after the flexoelectric measurements, which ranges from 1.8mm to 2.2mm.

Structural characterizations. The ice surface (Fig. S1a) was imaged under an optical microscope (NIKON ECLIPSE LV100D) with a temperature chamber (Linkam, HFS600E-PB4). Raman spectrum (Fig. S1c) was measured by a confocal Raman spectrometer (Witec Alpha300R) with the same Linkam chamber. The laser wavelength, power density, and grating

were 532 nm, 8 mW and 600 lines/mm⁻¹ respectively. X-ray diffraction patterns (Fig. S1d) were measured by a Diffractometer (X'pert Pro MPD Malvern-Panalytical) with a low-temperature chamber from Anton Paar (TTK600). The top electrode of the ice capacitor, grown in-situ in the temperature chamber using the same method described above, was removed from ice to enable these measurements.

Flexoelectric characterizations. A dynamic mechanical analyzer (Electroforce 3200, TA Instruments) was used to apply an oscillating 3-point bending deformation, which was recorded by a High Accuracy Displacement Sensor (HADS) embedded in the DMA. To reduce 1/f noise from the environment, relatively high drive frequencies (10~17 Hz) of the dynamic force were used, which is still far from the resonant frequency and so the loading can be regarded as a quasi-static condition. A small static force (typically -1.25N) was applied simultaneously to hold the sample in place.

The AC displacement δ at the sample's center measured by the HADS is converted to the average strain gradient across the electrode area by³³

$$\overline{\frac{\partial \varepsilon_{11}}{\partial x_3}} = \frac{12\delta}{L^3}(L - a), \quad (1)$$

where a is the half-length of the electrodes, L is the distance between two bottom ceramic bars. In our experimnts, L and a are 30mm and 15mm respectively. The bending-induced electric charge was converted by an amplifier (2692, Brüel & Kjær) to a voltage signal by a charge gain of 100mV/pC, which was then recorded with the bending displacement synchronously by an oscilloscope (MDO3104, Tektronix). The measured charge Q was converted to the average electric polarization across the electrode area along the thickness direction by

$$\overline{P_3} = \frac{Q}{A}, \quad (2)$$

where A is the area of the electrodes and equal to 30mm*5mm in our experiments. To exclude the environmental interferences, we performed the Fourier transformation on the recorded displacement δ and charge Q and used the first-harmonic signal for the calculations in equation (1) and (2). With the measured strain gradient and polarization, the effective flexoelectric coefficient is calculated by

$$\mu_{13}^{eff} = \overline{P}_3 / \overline{\frac{\partial \varepsilon_{11}}{\partial x_3}} \quad (3)$$

To further make sure what we are measuring is flexoelectricity rather than the environmental noise, we applied different forces to the sample and measured the corresponding induced charge. By doing a linear regression of the relationship between strain gradients and polarization, we extracted the slope value as the effective flexoelectric coefficient and the standard error value as the error bar (Fig. 1d). Every data point in Fig. 2a, Fig. 3b and Fig. S4, including its mean value and error bar, is calculated by such a linear regression.

Temperature-dependent measurements were achieved by competitive action of a resistive heater and a liquid N₂ bath. We started the flexoelectric measurements at ~223 K, well below the temperature at which ice-pre-melting and creeping plastic deformation can occur, but still well above the ferroelectric transition of the surface layer. From that temperature, we measured on cooling down to 143 K, followed by heating measurements all the way up to 273 K. To avoid the influence of the pyroelectric effect or any other interference, each measurement was performed at a fixed temperature instead of sweeping the temperature with a constant strain gradient. The temperature interval between each flexoelectric measurement was set to ~5 K and the flexoelectric coefficient at each temperature was measured by doing the least squares regression of the polarization as a function of strain gradient for five different applied strain gradients.

Ab Initio Simulations. We used the siesta code^{65,66} to perform DFT calculations within the generalized gradient approximation (GGA) to the exchange and correlation (XC) functional. The calculations use a combination of PBE⁶⁷ and vdW-DF(PBEx)^{68,69} functionals. These density functionals have previously been shown to give good results for the bulk XI-Ih phase transition^{70,71}. Relaxations are done using the same combination of parameters as described in⁷¹. For the free energy calculations which include the nuclear quantum effects, the vibrational modes are calculated using the frozen phonon approximation. We only compute the phonons for the bulk ices, and add to the free energy the classical energy of the ice-Au[111] interface. The proton order-to-disorder phase transition temperature is determined from the Helmholtz Free energy at zero pressure. We account for nuclear quantum effects in the bulk ices within

the quasi-harmonic approximation, with details provided in Supplementary S5(B). The main modification to the free energies of the bulk ices in this work arises from accounting for the zero-temperature interfacial binding energy contribution to the cohesive energy of ice. The computation of this energy is described in Supplementary S5(A).

Acknowledgments: We thank J. Liu for her code to process the experimental data, N. Domingo, D. Pesquera, M. Stengel for useful discussions, and P. Vales, J. M. Caicedo, D. Pesquera, S. Ganguly, J. Padilla for the technical support. This project is funded by the Spanish Ministry of Economy, Industry and Competitiveness (projects MAT2016-77100-C2-1-P), the Catalan AGAUR agency (project: 2017-SGR-579), and the National Natural Science Foundation of China (Grant No. 12090030). ICN2 is funded by the CERCA programme/Generalitat de Catalunya and by the Severo Ochoa programme (SEV-2017-0706). X.W. acknowledges the financial support from the China Scholarship Council. M.F.-S. and A.M. were funded by the U.S. Department of Energy, Office of Science, Basic Energy Sciences, under Award No. DE-SC0019394, as part of the CCS Program.

Author contributions: G.C. conceived the idea and coordinated this work. G.C. and X.W. designed the experiments. X.W. and Q.M. performed the experiments under the supervision of G.C. and S.S.. A.M. and M.F.-S. performed the *ab initio* calculations and associated data modeling. X.W. performed the calculations for the electrification analysis. X.W. and G.C. wrote the manuscript with the input from all the other authors. All authors discussed the results and commented on the manuscript.

Competing interests: Authors declare that they have no competing interests.

Data and materials availability: All data are available in the main text or the supplementary materials

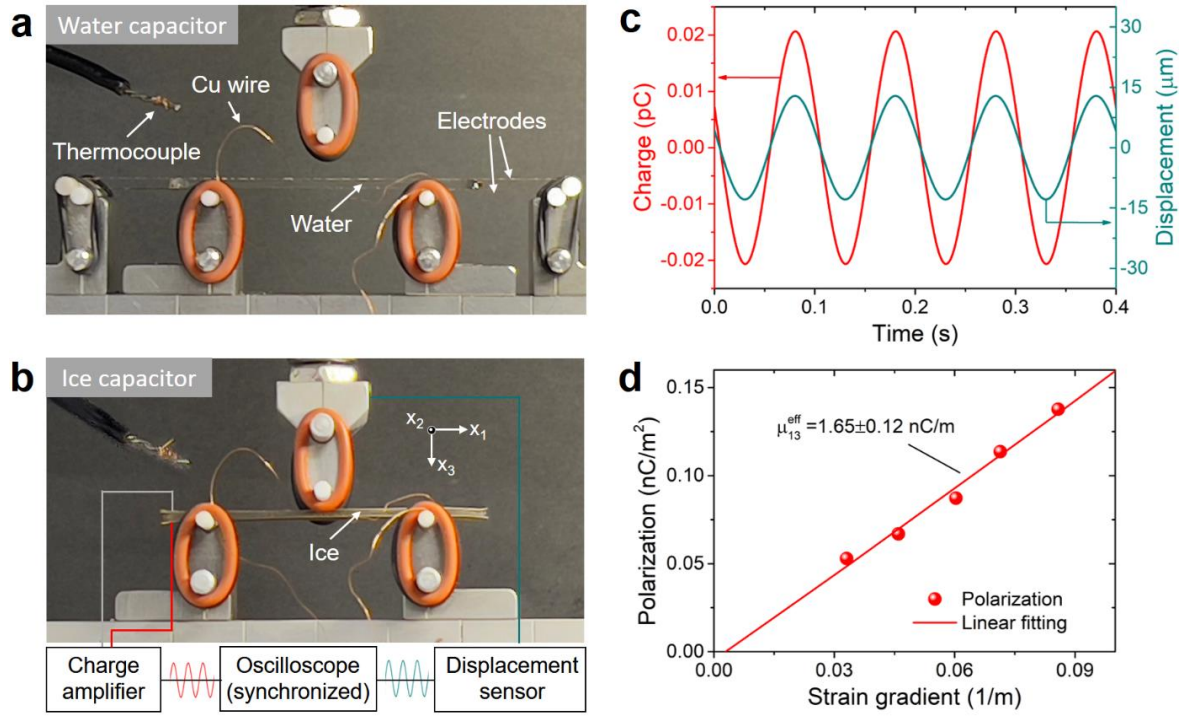


Fig. 1 Experimental setup for measuring ice flexoelectricity. **a**, A water capacitor, consisting of a layer of water and two pieces of Au electrodes. **b**, An ice capacitor placed in the DMA for oscillating three-point bending deformation. The displacement in the center and the bending-induced electric charge are recorded by an oscilloscope synchronously. **c**, Fourier-filtered first-harmonic displacement (the cyan curve) and charge (the red curve) for an applied displacement of $12.5 \mu\text{m}$. **d**, Electric polarization versus strain gradients, and linear fit to the results. The data in (c) and (d) was obtained at 237 K.

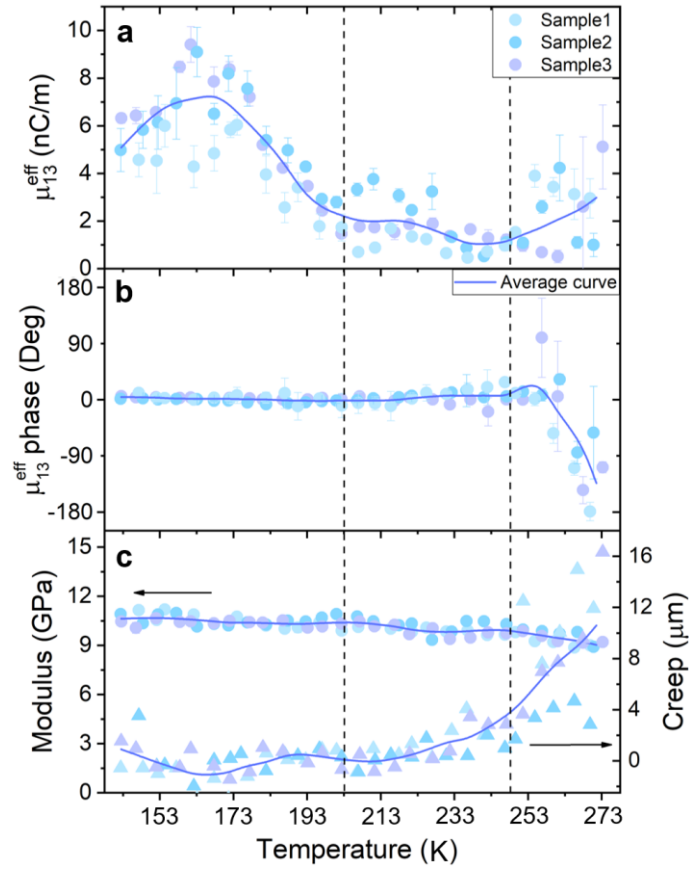


Fig. 2. Temperature dependence of ice flexoelectricity and mechanical properties. **a**, The effective flexoelectric coefficient as a function of temperature. **b**, The phase angle between displacement and polarization charge as a function of temperature. **c**, The modulus and the creep displacement in the first ten seconds of loading as a function of temperature. The data shown in this figure is obtained in three samples with Au electrodes. The solid lines represent the smoothed average curve. The error bars in (a) and (b) represents the standard error from linear regressions and the standard deviation from averages respectively.

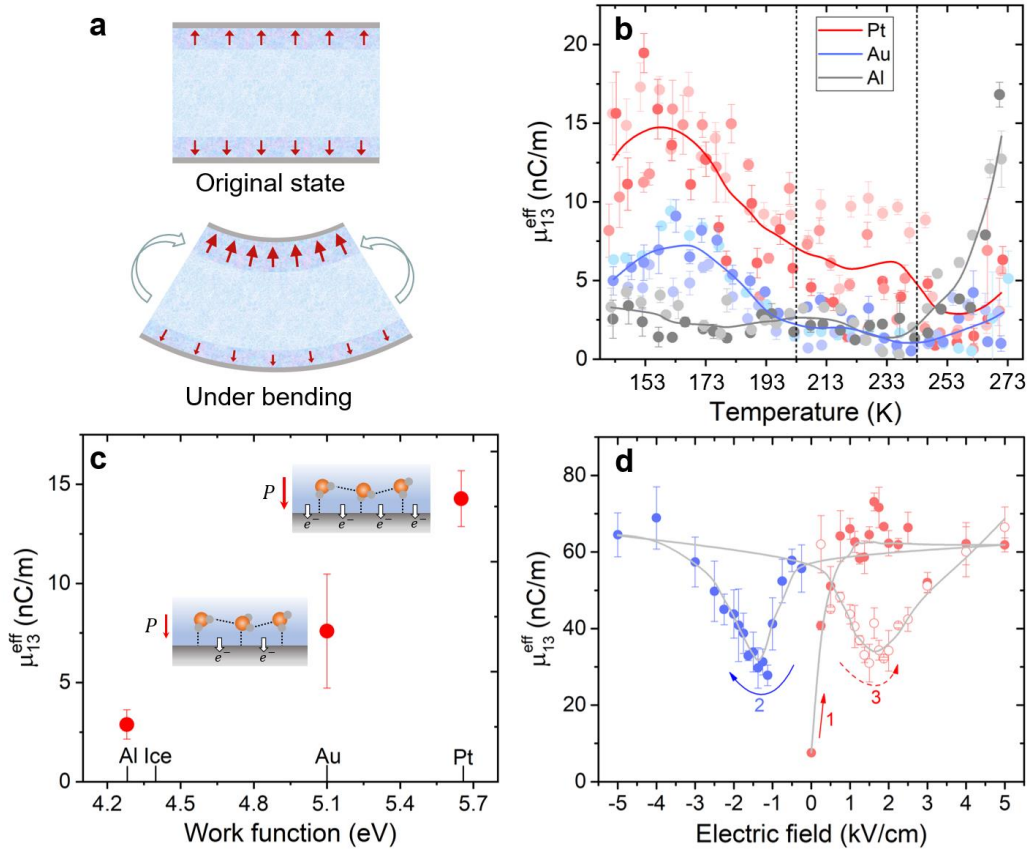


Fig. 3. Surface contribution to enhanced flexoelectricity. **a**, Schematic illustration of how surface polarization can contribute to effective flexoelectricity in a slab with polar surface layers. **b**, Experimental flexoelectric coefficient of ice with Pt, Au, and Al electrodes as a function of temperature. The solid lines are a smooth average of all the capacitors having the same type of electrode. The electrode-dependent results indicate a dependence of flexoelectricity on surface boundary condition. **c**, Value of the flexoelectricity at 163 K as a function of the electrode work functions. **d**, The evolution of flexoelectricity as a function of poling electric field measured at ~155K. The error bars in (b) represents the standard error from linear regressions. The error bars in (c) and (d) represent the standard deviation from averages of (c) different samples or (d) multiple measurements.

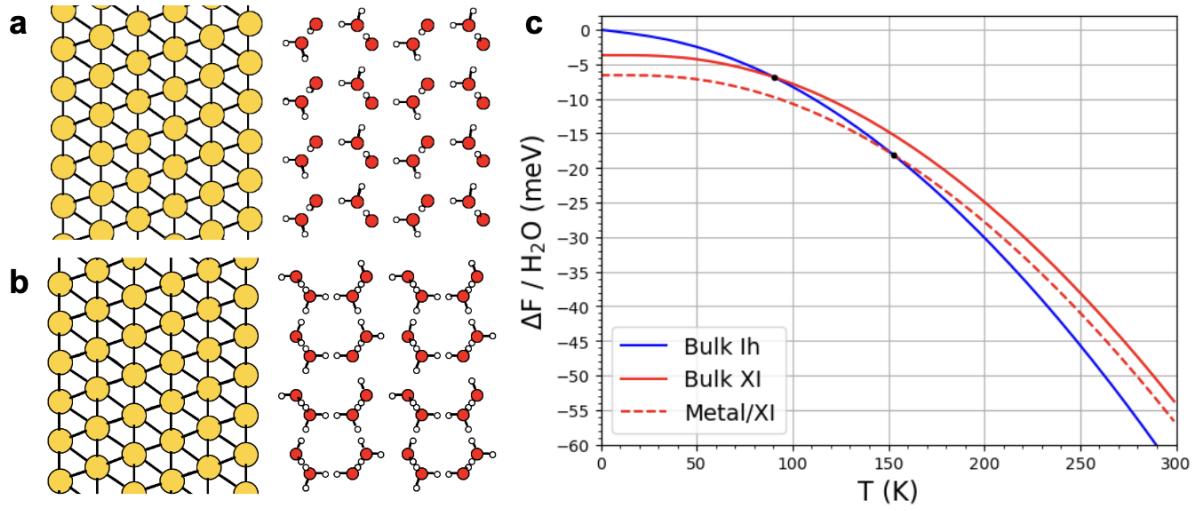


Fig. 4. *Ab initio* simulations of Au [111]-ice (Ih and XI) [001] interfaces. **a**, Illustration of IceXI/Au[111] system. **b**, Illustration of IceIh/Au[111] system. **c**, Relative free energy diagram for the ice XI and ice Ih, along with bulk calculations from previous work⁷¹. The dashed lines are rigid shift of the bulk XI curve when the interfacial energy is added to the bulk one. The result is an upward shift of the ferroelectric Curie temperature (at which the least-energy state changes from Ih to ice XI) to $T_c \sim 152$ K.

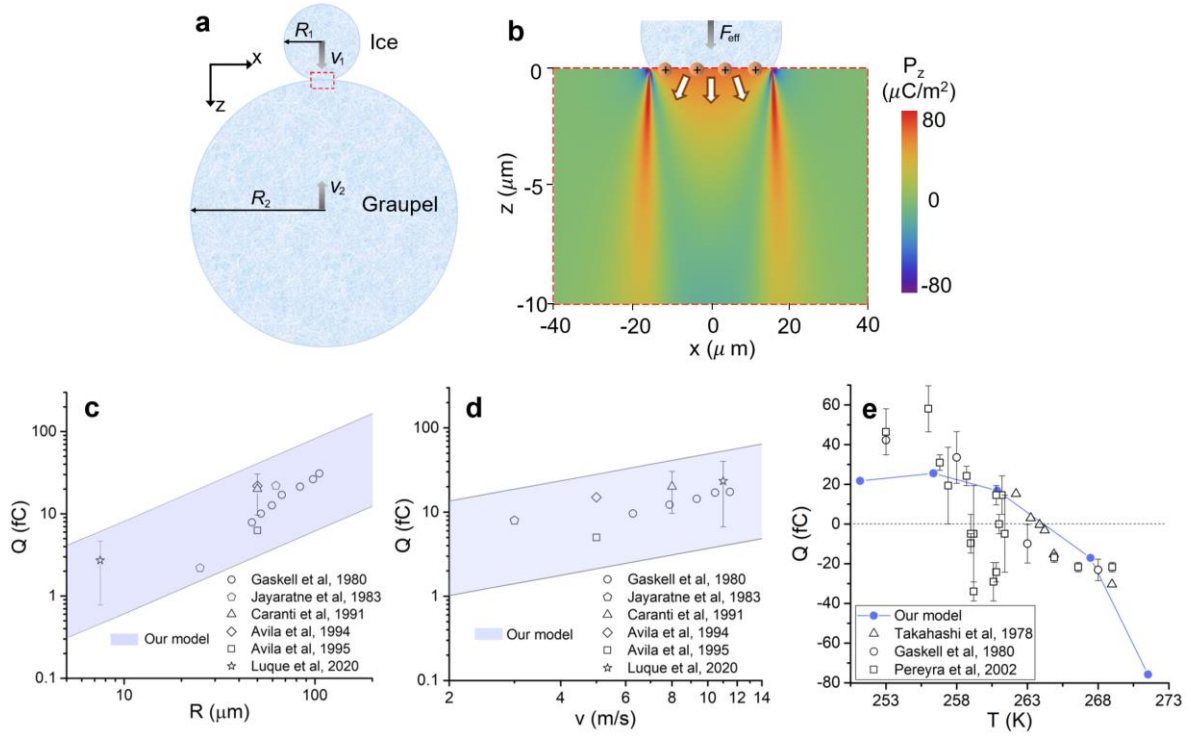


Fig. 5. Flexoelectricity in ice-electrification events. **a**, Schematic diagram of a typical collision between a small ice particle and a larger graupel. **b**, Calculated distribution of the vertical flexoelectric polarization beneath the indentation surface. The open arrows represent polarization. **c to e**, Dependence of contact-charge Q on particle radius, velocity, and temperature. The calculated results are compared with previous experiments^{56,58-64}, which are normalized for direct comparison (see details in Supplementary S7). Parameters used in calculation: (b) $R=50 \mu\text{m}$ ⁵⁸, $v=8 \text{ m/s}$ ⁵⁸, $Y_2=7 \text{ GPa}$ ^{3,72}, $\mu_{13}^{eff}=3 \text{ nC/m}$. (c) $v=8 \text{ m/s}$ ⁵⁸; $Y_2=1\sim 9 \text{ GPa}$ ^{3,72}; $\mu_{13}^{eff} = \mu_{13}^{eff}(263\text{K})$ from Fig. 3b; (d) $R=50 \mu\text{m}$ ⁵⁸, $Y_2=1\sim 9 \text{ GPa}$ ^{3,72}, $\mu_{13}^{eff} = \mu_{13}^{eff}(263\text{K})$ from Fig. 3b. (e) $R=50 \mu\text{m}$ ⁵⁸, $v=8 \text{ m/s}$ ⁵⁸, $Y_2=1 \text{ GPa}$, $\mu_{13}^{eff}=\max[\mu_{13}^{eff}(T)]*\cos(\varphi)$ where $\mu_{13}^{eff}(T)$ from Fig. 3b and φ from the sample1 phase angle in Fig. 2a.

Supplementary Information for

Flexoelectricity and surface ferroelectricity in water ice

Authors: X. Wen^{1,3}, Q. Ma¹, A. Mannino^{4,5}, M. Fernandez-Serra^{4,5}, S. Shen^{1*}, G. Catalan^{2,3*}

Affiliations:

¹State Key Laboratory for Strength and Vibration of Mechanical Structures, School of Aerospace Engineering, Xi'an Jiaotong University, Xi'an, China.

²ICREA—Institutio Catalana de Recerca i Estudis Avançats, Passeig Lluís Companys 23, Barcelona, Catalonia

³Institut Catala de Nanociencia i Nanotecnologia (ICN2), CSIC and The Barcelona Institute of Nanoscience and Technology (BIST), Campus Universitat Autònoma de Barcelona, Bellaterra, Catalonia.

⁴Physics and Astronomy Department, Stony Brook University, Stony Brook, New York 11794-3800, United States

⁵Institute for Advanced Computational Science, Stony Brook University, Stony Brook, New York 11794-3800, United States

*Corresponding author. Email: sshen@mail.xjtu.edu.cn; gustau.catalan@icn2.cat

S1. Excluding bending-induced phase transition

Pressure-induced phase transition in ice is a well-known effect, but it can be excluded in our experiments, because the actual stress at the surface is too small compared to the energies involved in structural phase transitions of ice. To illustrate this, we have performed a finite element simulation (COMSOL Multiphysics 5.3) using the same geometric parameters, material properties, and mechanical boundary conditions of our experiments. Fig. S6 shows the distribution of the in-plan stress σ_{11} across the beam under the maximum force (2.5N) used in our experiments. As expected, the beam experiences compression on one side and stretching on the other side; and the maximum bending-induced stress at the surface is ~ 0.005 GPa. This is orders-of-magnitude smaller than the pressure needed to induce a phase transition to ice IX (~ 0.2 GPa^{1,2}) or amorphization (~ 1 GPa³).

S2. Analysis of the contribution from grain boundaries

While indeed our samples are polycrystalline and grain boundaries are non-centrosymmetric, the grain-boundary contribution to the total flexoelectric effect can be neglected, both on theoretical and on experimental grounds. Theoretically, we must remember that at each grain boundary there are two opposing surfaces, corresponding to the adjacent grains. These surfaces have opposite orientation and, therefore, on average their surface-piezoelectric contributions must cancel each other. As indirect evidence, the flexoelectricity of BaTiO₃ and SrTiO₃ has been studied in ceramics^{4,5} and single crystals^{6,7}, finding no significant difference of flexoelectric coefficient, suggesting that the existence of grain boundaries in ceramics does not affect the flexoelectric outcome. To provide direct experimental evidence for lack of grain boundary contributions, we have performed new flexoelectric experiments with different grain sizes, achieved by annealing the sample for different durations at 267 K, during which ice grains recrystallized and changed grain sizes (Fig. S7a~c). All flexoelectric measurements fell into the range of 1~3 nC/m (Fig. S7d) as we summarized in the manuscript, and no conclusive effect of grain size on ice flexoelectricity was observed.

S3. Ab initio calculation of the piezoelectric constant of ice XI

The unit cell for this calculation is an ice XI unit cell with 4 water molecules. The exchange-correlation functional is VDW/DRSLL. The lattice vectors have the following form: $[0, a, 0], [a\sqrt{3}/2, a/2, 0], [0, 0, c]$ with lattice parameters a and c . First, we adjust c with a fixed lattice constant, a , and run a SIESTA calculation that allows the “out-of-plane” H atoms to relax. We then determine the most energetically favorable configuration and repeat this for several values of a (Fig. S9a). Mulliken charges for each atom in the system are computed by SIESTA, and we use them to calculate the polarization in the c -direction. Finally, we plot the polarization as a function of the strain on the lattice constant (Fig. S9b). The slope of this plot is the transverse piezoelectric constant e_{13} , which was found to be 0.32 C/m^2 .

S4. Surface piezoelectricity

Fig. 3a schematically shows how surface ferroelectricity can contribute to effective flexoelectricity. In a dielectric sample with polar skin layers at the surface, the surface-piezoelectric contribution to the total effective flexoelectricity is^{8,9}

$$\mu_{13}^{eff} = e_{13}^{surf} \lambda \frac{h\epsilon_b}{2\lambda\epsilon_b + h\epsilon_\lambda} \quad (\text{S1})$$

where e_{13}^{surf} is the transverse surface piezoelectric constant, λ and h are the thickness of the skin layer and the bulk, ϵ_λ and ϵ_b are the dielectric constant of the skin layer and the bulk respectively. When λ is much thinner than h ($\frac{\lambda}{h} \ll 1$), equation (S1) can be simplified as

$$\mu_{13}^{eff} = e_{13}^{surf} \lambda \frac{\epsilon_b}{\epsilon_\lambda} \quad (\text{S2})$$

By subtracting the bulk contribution ($\sim 2 \text{ nC/m}$) from the measured flexoelectric peak ($\sim 7.6 \text{ nC/m}$), we can obtain a surface-contributed μ_{13}^{eff} of $\sim 5.6 \text{ nC/m}$ in Au-electrodes samples. $e_{13}^{surf} = 0.32 \text{ C/m}^2$ is obtained in Section 3 by ab initio calculations. We assume that the dielectric constant of the skin layer is similar to that of the bulk, i.e., $\epsilon_b/\epsilon_\lambda = 1$. Substituting these parameters in equation (S2), we estimate the skin-layer thickness λ at Au/ice interface to be $\sim 17.5 \text{ nm}$.

According to equation (S2), the effective flexoelectric coefficient only depends on the thickness of the skin layer λ , and is independent from the bulk sample thickness h . As

demonstrated in previous works^{10,11}, the flexoelectric coefficient can only be proportional to sample thickness when the samples are semiconductors with Schottky junctions, which is not the case for ice. The independence on bulk thickness may seem counter-intuitive for a claimed surface property, but it is in fact reasonable. When a beam is bent with a given curvature, increasing sample thickness linearly reduces the surface/volume ratio but, at the same time, linearly increases the surface strain. The two opposite dependencies mutually cancel, resulting in no bulk thickness dependence. This conclusion has been affirmed in the theoretical literature^{8,9} and is backed by our own flexoelectric measurements for samples with different thicknesses (from 1mm to 2mm), as shown in Fig. S10 below.

S5. Ab initio calculation of relative energy between ice XI and ice Ih with Au[111] interface

A. Cohesive energy calculations at T=0

Simulating these systems and being able to compare them is not trivial due to the polar nature of the ice XI phase. The limitations on the size of the system that can be computationally accessible poses a general problem when studying water or ice interfacial properties using ab initio simulations. In the case of ice XI, two different options to study the interface are presented in Fig. S11. These are non-ideal. In the case of (a) two different interfaces with the metal are computed in one calculation. One with the protons facing the metal and (positive end of the polarized slab) and one with the O atoms facing the metal (negative end of the slab). The polarization is screened by the metal, but it is difficult to separate the contributions from the two interfaces. It is possible to create a proton ordered slab with symmetric interfaces as in (b), both of them with the presumed favorable H-Metal interface. However, in order to do this one needs to create a layer of H-bond defects in the middle of the slab. These are water molecules not completely satisfying Bernal–Fowler–Pauling ice rules (There is always a proton in between each pair of oxygen atoms and each oxygen always keeps two close, covalently bound protons). When comparing these structures to a proton disordered system (which always has, by definition, symmetric interfaces), the proton disordered system will always be more stable. Hence it is necessary to account for the defect formation energy, and this makes the calculation much more complicated. We can calculate the cohesive energy per water molecule with the following equation:

$$E_{Cohesive/H_2O} = E_{Ice/Au} - E_{(Ice-H_2O)/Au} - E_{H_2O} \quad (S3)$$

with the subscripts denoting which species are included in the calculation. In the second term, we remove a single water molecule from the surface layer of the ice. The unit cell and all other simulation parameters remain the same.

This calculation is done for system (b) and a similar system (c) with ice Ih. The difference in cohesive energy for these two systems is 233 meV with system (b) being more favorable. We also do this calculation for bulk ice XI and bulk ice Ih without the Au slab. The difference in cohesive energy for these two systems is 93 meV with the bulk ice XI system being more favorable. We conclude from this that the Au interface creates an enhanced stability of 140 meV. As the number of ice bilayers increases, we anticipate this enhanced stability will be proportional to the surface-to-volume ratio. From our previous work¹², we have shown that the bulk limit for the relative energy per water molecule between ice XI and ice Ih is 3.68 meV. The final energy calculation at 0 K is as follows:

$$E_{Relative/H_2O}^{T=0} = \frac{-140 \text{ meV}}{N_{Bilayers}} - 3.68 \text{ meV} \quad (S4)$$

B. Free energy differences versus Temperature

The treatment of nuclear quantum effects will be summarized here and is described in full detail in our previous work¹². We define V_0 to be the volume that minimizes the Born-Oppenheimer energy, $E_0(V)$. We can expand this energy in a Taylor series for small perturbations from V_0 .

$$E_0(V) = E_0(V_0) + \frac{B_0}{2V_0} (V - V_0)^2 \quad (S5)$$

The phonon frequencies can also be expanded in this way.

$$\omega_k(V) = \omega_k(V_0) \left(1 - \gamma_k \frac{V - V_0}{V_0} \right) \quad (S6)$$

In these expansions, B_0 is the dominant part of the bulk modulus with vibrational corrections removed. γ_k are the mode Grüneisen parameters, defined as

$$\gamma_k = -\frac{\partial(\ln \omega_k)}{\partial(\ln V)} = -\frac{V}{\omega_k} \frac{\partial \omega_k}{\partial V}. \quad (S7)$$

We calculate the phonon frequencies, ω_k , at three different volumes and calculate its volume dependence to linear order. This adds a volume dependence to the Helmholtz free

energy $F(V, T)$ ¹³ of independent harmonic oscillators.

$$F(V, T) = E_0(V) + \sum_k \left[\frac{\hbar \omega_k(V)}{2} + k_B T \ln(1 - e^{-\hbar \omega_k(V)/k_B T}) \right] - TS_H \quad (S8)$$

The sum is over both phonon branches and phonon wave vectors within the Brillouin zone.

The entropy of the proton disorder, S_H , is included in the last term of the free energy equation. This entropy is zero for ice XI (proton-ordered ice). Pauli has estimated that the entropy for ice Ih (proton-disordered ice) is $Nk_B \ln(3/2)$, which was obtained theoretically¹⁴ and experimentally^{15,16}.

We can find the classical limit of the free energy by taking the high-temperature limit of (S8).

$$F(V, T) = E_0(V) + \sum_k \left(k_B T \ln \left\{ \frac{\hbar \omega_k[V(T)]}{k_B T} \right\} \right) - TS_H \quad (S9)$$

In Fig 4c of the manuscript, we show the free energies of bulk ice Ih and bulk ice XI as a function of temperature. The difference between these two free energies should match the enhanced stability described in the previous section at the transition temperature.

$$\Delta F_{(XI-Ih)/H_2O}(T_C) = -(E_{Relative/H_2O}^{T=0} + 3.68 \text{ meV}) \quad (S10)$$

The skin layer thickness, h , can be found from the number of bilayers with the conversion factor 0.3615 nm / 1 bilayer. After combining (S4) and (S10), we are left with the following equation:

$$h(T_C) = \frac{140 \text{ meV} \cdot 0.3615 \text{ nm}}{\Delta F_{(XI-Ih)/H_2O}(T_C)} \quad (S11)$$

Substituting the obtained skin-layer thickness in Section 4 into equation (S11), we find T_C to be ~152K, in agreement with the experimental results.

S6. Calculation of flexoelectric polarization and field

Flexoelectric polarization is defined as^{17,18}

$$P_i = \mu_{ijkl} \frac{\partial \varepsilon_{kl}}{\partial x_j} \quad (S12)$$

where μ_{ijkl} is the fourth-rank tensor of flexoelectric coefficients, P_i is the electric polarization, ε_{kl} is the strain tensor, and x_j is the position coordinate. We consider three

components of μ_{ijkl} (longitudinal μ_{1111} , transversal μ_{1122} , and shear μ_{1212}) in our calculations, which can be rewritten in the Voigt notation as μ_{11} , μ_{12} , and μ_{44} , respectively. The polarization field in Cartesian coordinates can be written as^{19,20}

$$\begin{aligned} P_x &= \mu_{11} \frac{\partial \varepsilon_{xx}}{\partial x} + \mu_{12} \left(\frac{\partial \varepsilon_{yy}}{\partial x} + \frac{\partial \varepsilon_{zz}}{\partial x} \right) + 2\mu_{44} \left(\frac{\partial \varepsilon_{xy}}{\partial y} + \frac{\partial \varepsilon_{xz}}{\partial z} \right) \\ P_y &= \mu_{11} \frac{\partial \varepsilon_{yy}}{\partial y} + \mu_{12} \left(\frac{\partial \varepsilon_{xx}}{\partial y} + \frac{\partial \varepsilon_{zz}}{\partial y} \right) + 2\mu_{44} \left(\frac{\partial \varepsilon_{xy}}{\partial x} + \frac{\partial \varepsilon_{yz}}{\partial z} \right) \\ P_z &= \mu_{11} \frac{\partial \varepsilon_{zz}}{\partial z} + \mu_{12} \left(\frac{\partial \varepsilon_{xx}}{\partial z} + \frac{\partial \varepsilon_{yy}}{\partial z} \right) + 2\mu_{44} \left(\frac{\partial \varepsilon_{xz}}{\partial x} + \frac{\partial \varepsilon_{yz}}{\partial y} \right) \end{aligned} \quad (S13)$$

Since it is not possible to measure separately each of the tensor components, we set μ_{11} , μ_{12} , and μ_{44} equal to the measured μ^{eff} and obtain the flexoelectric polarization from equation (S13) using the calculated strain gradients (see the next section).

In polarizing the material, flexoelectricity acts as an effective electric field²¹. The flexoelectric field in isotropic solids (relative permittivity ξ_r is a constant) is given by^{17,18}

$$E_x = \frac{P_x}{\xi_0 (\xi_r - 1)}, \quad E_y = \frac{P_y}{\xi_0 (\xi_r - 1)}, \quad E_z = \frac{P_z}{\xi_0 (\xi_r - 1)} \quad (S14)$$

S7. Calculation of flexoelectricity in the contact region of ice collisions.

The classical Hertzian theory of contact mechanics²² has been widely used to estimate the strain distributions and the associated flexoelectricity in contact problems²³⁻²⁵. Since the size of ice particles (R_1) is often orders of magnitude larger than that (R_2) of graupel particles^{26,27}, we treat the ice particle as an indenter with radius of R and treat the graupel particle as a semi-infinite elastic space. Then we can adopt Hertzian theory to calculate the strain distributions in graupel particles under the indentation of the small ice particle. To do so, we need to convert the impact of the indenter on the semi-space to an effective force F_{eff} by²⁸

$$F_{\text{eff}} = \frac{4}{3} Y_{\text{eff}} \sqrt{R} \left(\frac{15 m v_r^2}{16 Y_{\text{eff}} \sqrt{R}} \right)^{3/5} \quad (S15)$$

where Y_{eff} is the effective Young's modulus of the contact, v_r is the relative velocity of the indenter moving toward the self-half space, m is the mass of the indenter which is equal to $\frac{4}{3}\rho\pi R^3$ (ρ refers to the mass density). Y_{eff} is given by²²

$$\frac{1}{Y_{eff}} = \frac{1-\nu_1^2}{Y_1} + \frac{1-\nu_2^2}{Y_2} \quad (S16)$$

where Y_1 , Y_2 and ν_1 , ν_2 are the Young's modulus and Poisson's ratio of the indenter and the semi-space, respectively. Under load F_{eff} , the contact radius a and mean pressure P_m on the contact surface can be expressed as²²

$$a = \sqrt[3]{\frac{3 F_{eff} R}{4 Y_{eff}}}, \quad P_m = \frac{F_{eff}}{\pi a^2} \quad (S17)$$

The stress fields of the semi-space beneath the contact region of a spherical indenter in cylindrical coordinates are given by²²

$$\sigma_{rr} = \frac{3p_m}{2} \left\{ \frac{1-2\nu}{3} \frac{a^2}{r^2} \left[1 - \left(\frac{z}{\sqrt{u}} \right)^3 \right] + \left(\frac{z}{\sqrt{u}} \right)^3 \frac{a^2 u}{u^2 + a^2 z^2} + \frac{z}{\sqrt{u}} \left[u \frac{1-\nu}{a^2 + u} + (1+\nu) \frac{\sqrt{u}}{a} \tan^{-1} \frac{a}{\sqrt{u}} - 2 \right] \right\} \quad (S18)$$

$$\sigma_{\theta\theta} = -\frac{3p_m}{2} \left\{ \frac{1-2\nu}{3} \frac{a^2}{r^2} \left[1 - \left(\frac{z}{\sqrt{u}} \right)^3 \right] + \frac{z}{\sqrt{u}} \left(2\nu + u \frac{1-\nu}{a^2 + u} - (1+\nu) \frac{\sqrt{u}}{a} \tan^{-1} \frac{a}{\sqrt{u}} \right) \right\} \quad (S19)$$

$$\sigma_{zz} = -\frac{3p_m}{2} \left\{ \left(\frac{z}{\sqrt{u}} \right)^3 \frac{a^2 u}{u^2 + a^2 z^2} \right\} \quad (S20)$$

$$\sigma_{rz} = -\frac{3p_m}{2} \left(\frac{rz^2}{u^2 + a^2 z^2} \right) \left(\frac{a^2 \sqrt{u}}{a^2 + u} \right) \quad (S21)$$

where u is the displacement of points on the contact surface, and can be expressed as

$$u = \frac{1}{2} \left[(r^2 + z^2 - a^2) + \sqrt{(r^2 + z^2 - a^2)^2 + 4a^2 z^2} \right] \quad (S22)$$

The strain beneath the contact region in cylindrical coordinates can be expressed by the isotropic Hooke's law

$$\begin{aligned}
\varepsilon_{rr} &= \frac{1}{Y} [\sigma_{rr} - \nu(\sigma_{\theta\theta} + \sigma_{zz})] \\
\varepsilon_{\theta\theta} &= \frac{1}{Y} [\sigma_{\theta\theta} - \nu(\sigma_{rr} + \sigma_{zz})] \\
\varepsilon_{zz} &= \frac{1}{Y} [\sigma_{zz} - \nu(\sigma_{rr} + \sigma_{\theta\theta})] \\
\varepsilon_{rz} &= \frac{1+\nu}{Y} \sigma_{rz}
\end{aligned} \tag{S23}$$

According to equation (S13) and the axial symmetry in this problem, the vertical polarization P_z beneath the contact region can be written in cylindrical coordinates as

$$P_z = \mu_{11} \frac{\partial \varepsilon_{zz}}{\partial z} + \mu_{12} \left(\frac{\partial \varepsilon_{rr}}{\partial z} + \frac{\partial \varepsilon_{\theta\theta}}{\partial z} \right) + 2\mu_{44} \frac{\partial \varepsilon_{rz}}{\partial r} \tag{S24}$$

Combining equations (S15) to (S24) and adopting typical parameters in an ice-collision event (Table S1), we have computed the distributions of the flexoelectric polarization beneath the indentation surface analytically, as shown in Fig. 5b. Integrating P_z over the contact area, we have further calculated the flexoelectric surface charge Q , and its dependences on particle radius, velocity, and temperature, as shown in Fig. S12 and Fig. 5c~e.

Despite numerous papers about ice-collision-induced charge separation, it is not easy to directly compare theoretical model and experiments, as the latter were usually reported under different experimental conditions that were not always fully described and/or where more than one experimental parameter was changed. In our manuscript, we selected eight experimental papers²⁹⁻³⁶, published from 1978 to 2020, to compare with our theory controlling for each variable separately. Gaskell's classic work³⁰, which had the best-described experimental conditions, was selected as a benchmark for comparison with the following parameters: $R=50 \mu\text{m}$, $v=8 \text{ m/s}$, $T=263 \text{ K}$. To investigate the effect of particle size R on the contact-electrification charge Q (Fig. 5c), we use our model to extrapolate experiments with different velocities³¹⁻³⁵ (at $\sim 263 \text{ K}$) to obtain a normalized Q at the reference velocity $v=8 \text{ m/s}$ for comparison. Similarly, to calculate the dependence of Q on velocity (Fig. 5d), we extrapolated these experiments³¹⁻³⁵ (at $\sim 263 \text{ K}$) with different particle size R to obtain a standardized Q at the reference radius $R=50 \mu\text{m}$ for comparison. Last, as for temperature dependence (Fig. 5e), we extrapolated these experiments^{29,36} with different particle sizes and velocities to obtain a standardized Q at $v=8$

m/s and $R=50\mu\text{m}$ for comparison. Note that these papers used diameter as particle size, but here we convert them to radius unit.

S8. Calculation of the flexoelectricity around a crack apex.

Around cracks, flexoelectricity is known to be large enough to influence physical properties like fracture toughness^{37,38} and even physiological ones such as bone-cell stimulation³⁹. At the same time, ice fractures are thought to cause electrification in polar regions^{40,41}. Here below we calculate the crack-induced flexoelectric field of ice.

For isotropic solids (such as polycrystalline ice), the elastic constants can be represented by two independent parameters⁴², i.e. Young's modulus Y and Poisson's ration ν . Under plane strain conditions, the linear elastic stress fields near a model I crack in Polar coordinates can be analytically expressed as⁴³

$$\begin{aligned}\sigma_{xx} &= \frac{K_I}{\sqrt{2\pi r}} \cos \frac{\theta}{2} \left(1 - \sin \frac{\theta}{2} \sin \frac{3\theta}{2} \right) \\ \sigma_{yy} &= \frac{K_I}{\sqrt{2\pi r}} \cos \frac{\theta}{2} \left(1 + \sin \frac{\theta}{2} \sin \frac{3\theta}{2} \right) \\ \sigma_{xy} &= \frac{K_I}{\sqrt{2\pi r}} \cos \frac{\theta}{2} \sin \frac{\theta}{2} \cos \frac{3\theta}{2} \\ \sigma_{zz} &= \nu (\sigma_{xx} + \sigma_{yy})\end{aligned}\tag{S25}$$

where K_I is the stress intensity factor, which can be generally expressed as⁴³

$$K_I = F \sigma_a \sqrt{\pi l}\tag{S26}$$

where σ_a is the applied stress, l is the length of the crack, F is the geometry factor of the specimen. K_I is directly proportional to the applied stress σ_a . When K_I increases to the critical value K_{IC} (fracture toughness), the model I crack starts to propagate. The plane strain is related to stress by the isotropic Hooke's law⁴²

$$\begin{aligned}
\varepsilon_{xx} &= \frac{1}{Y} \left[\sigma_{xx} - \nu (\sigma_{yy} + \sigma_{zz}) \right] \\
\varepsilon_{yy} &= \frac{1}{Y} \left[\sigma_{yy} - \nu (\sigma_{xx} + \sigma_{zz}) \right] \\
\varepsilon_{xy} &= \frac{1+\nu}{Y} \sigma_{xy}
\end{aligned} \tag{S27}$$

We substitute equation (S25) into equation (S27) for calculations in *Mathematica*. Let K_I equal to K_{IC} (see Table S1), we have computed analytically the distributions of strain and the strain gradients near a propagating crack apex. Substituting the calculated strain gradients into equation (S13) and (S14), we have computed the crack-tip flexoelectric field analytically, as shown in the 2D maps in Fig. S13a. As expected, the flexo-electric field is largest at the crack tip, reaching up to ~ 1 MV/m and decaying progressively away. We can further compare these calculations to the classic experiment by Petrenko et al⁴⁴, who measured the electrical potential of ice (at $T=263$ K) in the vicinity of a stable crack under uniaxial tension (Fig. S13b) and reported the peak value of 0.8 mV at $r=1$ mm.

For an edge crack with the specimen geometry depicted in Fig. S13b, K_I is given by⁴⁵

$$K_I = \left[1.122 - 0.231 \frac{l}{w} + 10.55 \left(\frac{l}{w} \right)^2 - 21.71 \left(\frac{l}{w} \right)^3 + 30.382 \left(\frac{l}{w} \right)^4 \right] \sigma_a \sqrt{\pi l} \tag{S28}$$

where W is the specimen width. Substituting the parameters (l, W, σ_a , see Table S1) used in the literature⁴⁴ into equation (S28), we have calculated K_I to be $92.4 \text{ kPa m}^{1/2}$, smaller than the fracture toughness K_{IC} ($108.5 \text{ kPa m}^{1/2}$). This is reasonable because the experiment in the literature⁴⁴ was on a stable crack, rather than a propagating crack. Using the calculated K_I , we again calculate the flexoelectric field near the crack tip. As shown in Fig. 14b, the bottom of the specimen was grounded, namely, $V(y = -65\text{mm}) = 0$. Therefore, the electric potential in the specimen can be calculated from the vertical component of flexoelectric field E_y by

$$V(x, y) = - \int_{-65\text{mm}}^y E_y(x, y) dy \tag{S29}$$

The experiment by Petrenko⁴⁴ was performed at 263 K, our measured flexoelectric coefficient at this temperature ranges from 2.1~8.0 nC/m in samples with different electrodes

(Fig. 3b). Let $x = 0$ and $y = -1\text{mm}$, the surface potential $V(0, -1\text{mm})$ is calculated to be $0.57 \sim 2.1 \text{ mV}$, in agreement with the reported value $\sim 0.8 \text{ mV}^{44}$.

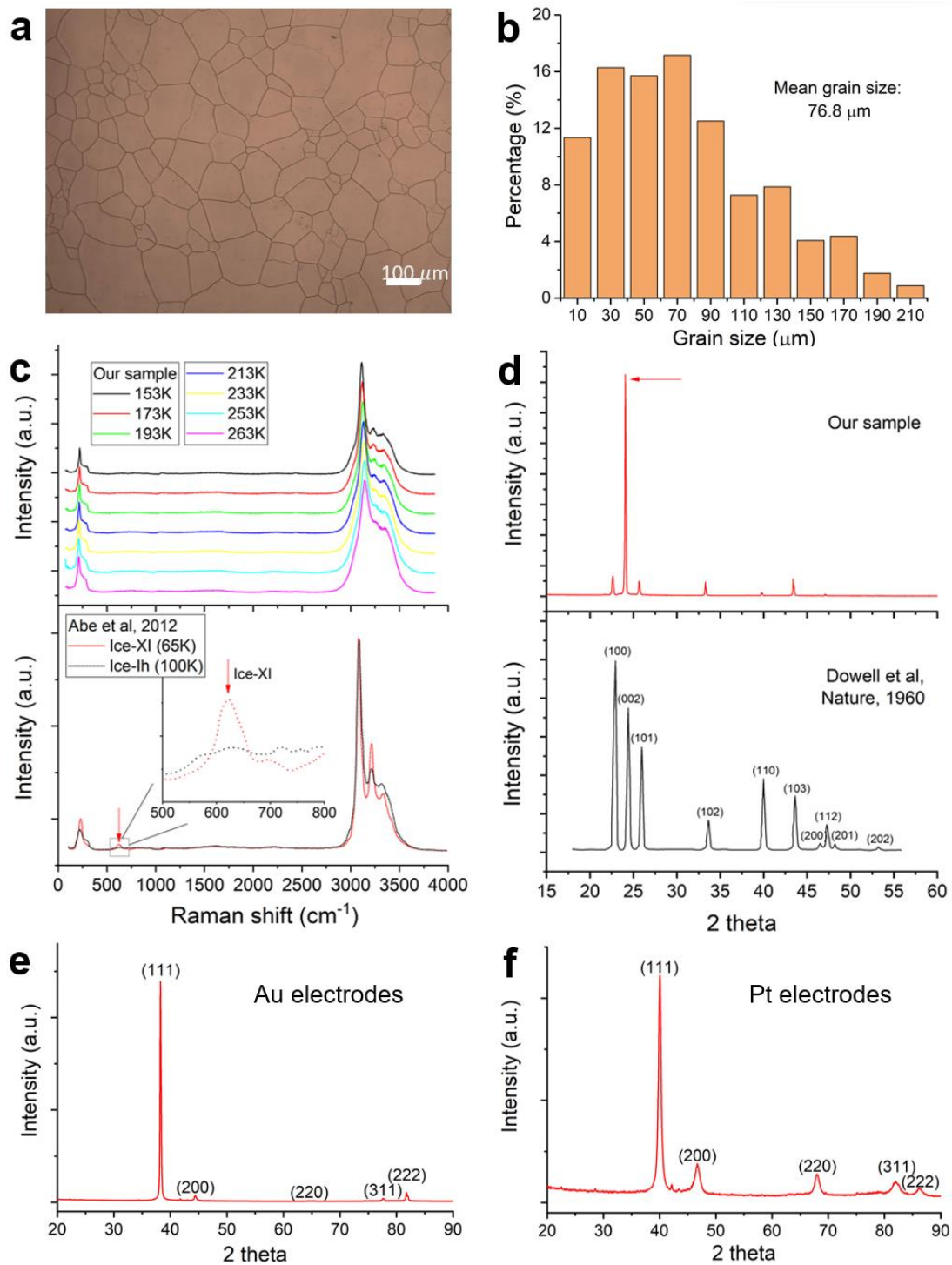


Fig. S1. Structural characterizations of our ice sample. **a**, Optical image of the sample surface. **b**, The statistical distribution of the grain size. **c**, The Raman spectrum measured at different temperatures, compared with the reported Raman spectrum for ice-Ih and ice-XI⁴⁶. **d**, The X-ray diffraction pattern measured at 256 K, compared with the reported Xrd pattern for ice-Ih⁴⁷. **e and f**, The X-ray diffraction pattern of Au and Pt electrodes respectively.

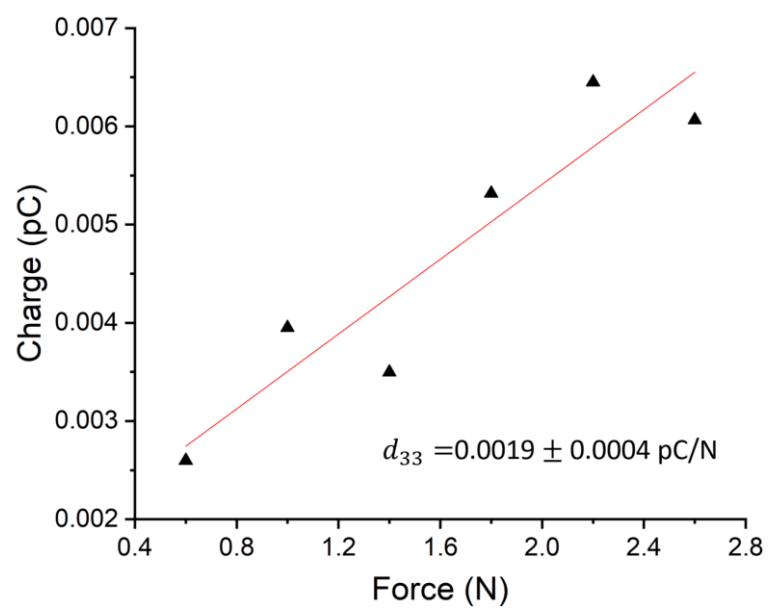


Fig. S2. Polarization charge versus the applied force in uniaxial compression experiments measured at $\sim 233 \text{ K}$

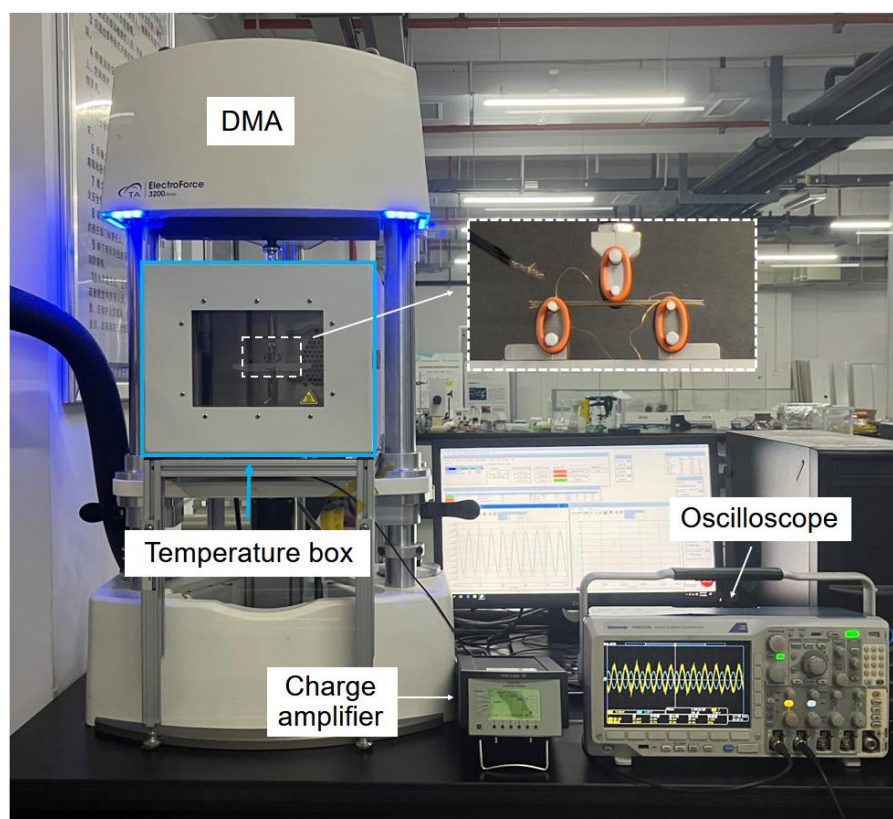


Fig. S3. Experimental setup, consisting of a dynamic mechanical analyzer (DMA) with temperature function, a charge amplifier, and an oscilloscope

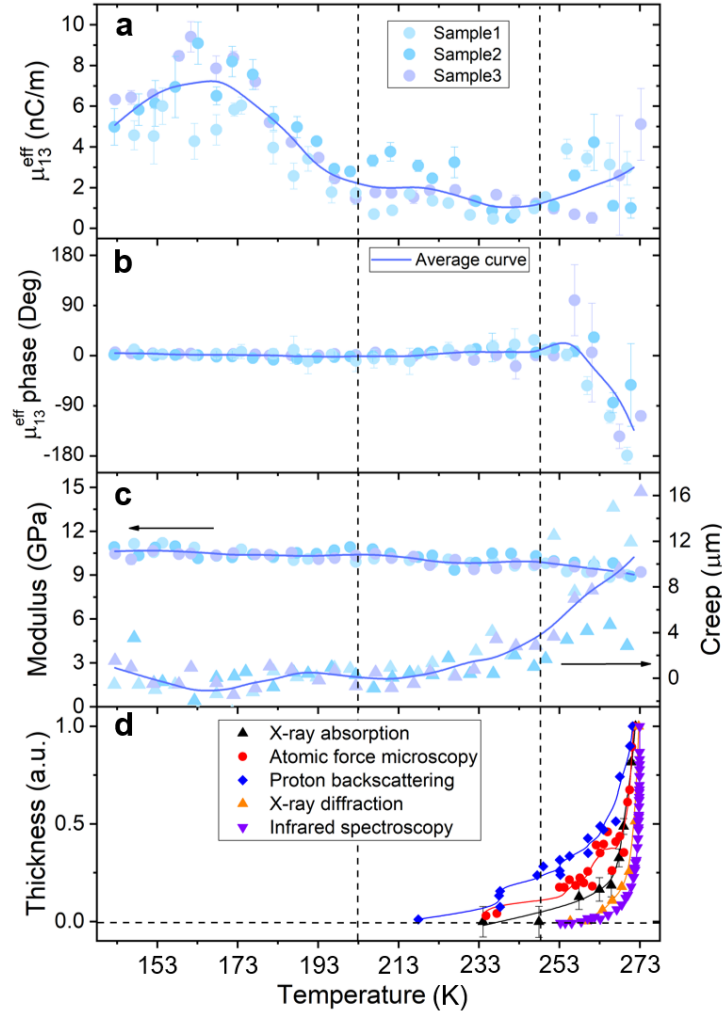


Fig. S4. **a**, The flexoelectric coefficient with Au electrodes versus temperature. **b**, The phase angle between displacement and polarization charge with Au electrodes versus temperature. **c**, The modulus and the creep displacement in the first ten seconds of loading versus temperature. **d**, The reported QLL thickness versus temperature measured with different techniques: X-ray absorption⁴⁸, Atomic force microscopy⁴⁹, Proton backscattering⁵⁰, X-ray diffraction⁵¹, Infrared spectroscopy⁵². The maximum QLL thickness is normalized to better show the temperature dependence.

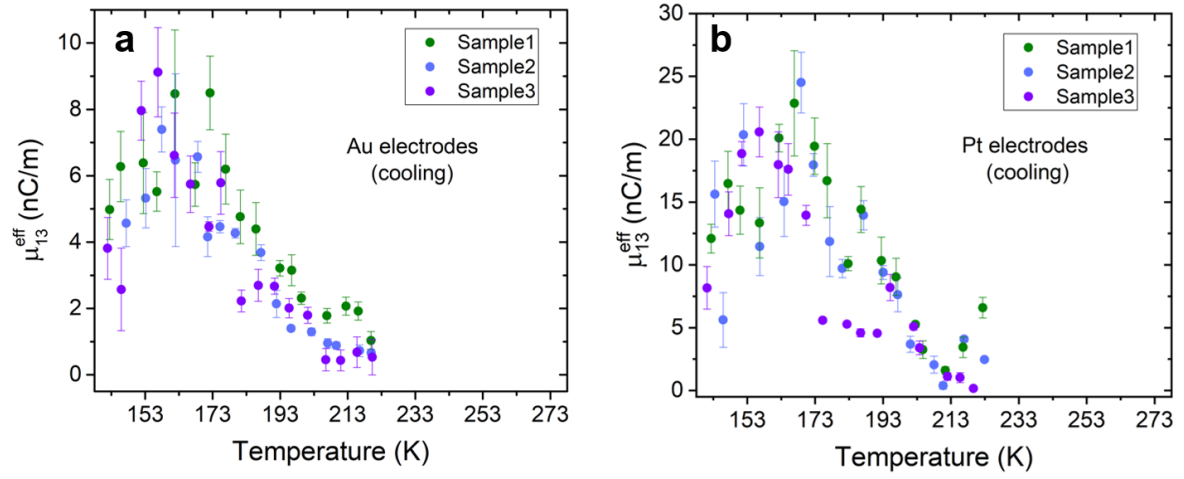


Fig. S5. The flexoelectric coefficient measured on cooling for samples with (a) Au electrodes and (b) Pt electrodes. The error bars represent the standard error from linear regressions.

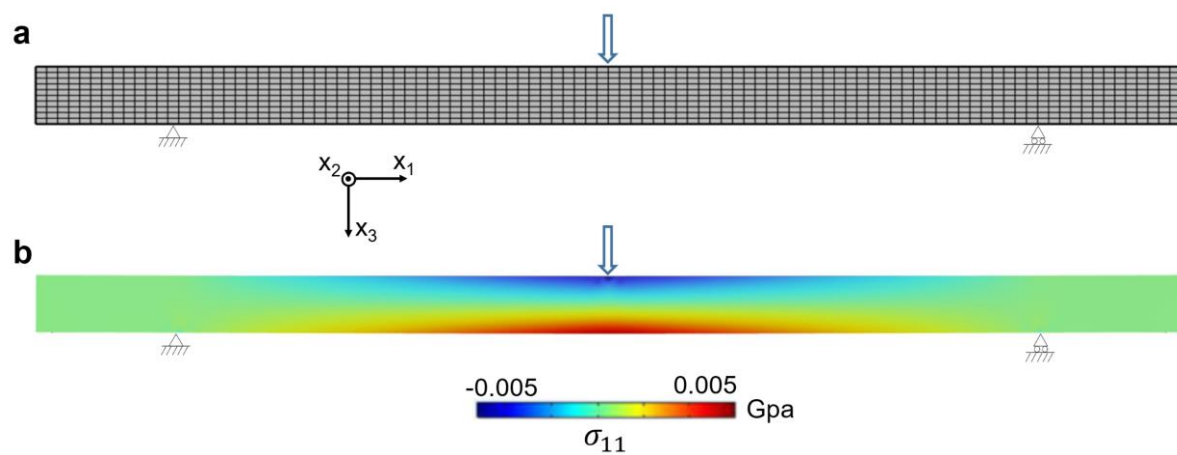


Fig. S6. Finite-element simulation of stress distribution in our sample under the maximum force (-2.5N).

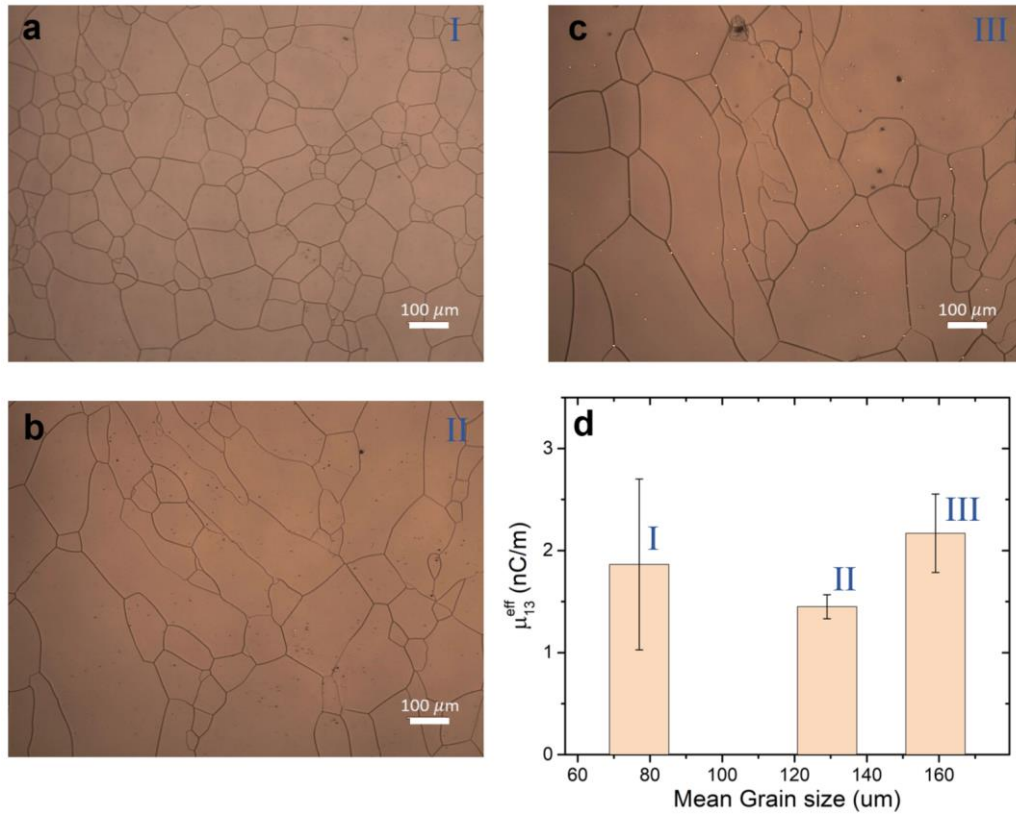


Fig. S7. Optical image of the grains on the surface of our ice sample (a) before annealing, (b) after annealing for half hour at 267 K and (c) after annealing for one hour at 267 K. d, The grain-size dependence of the flexoelectric coefficient

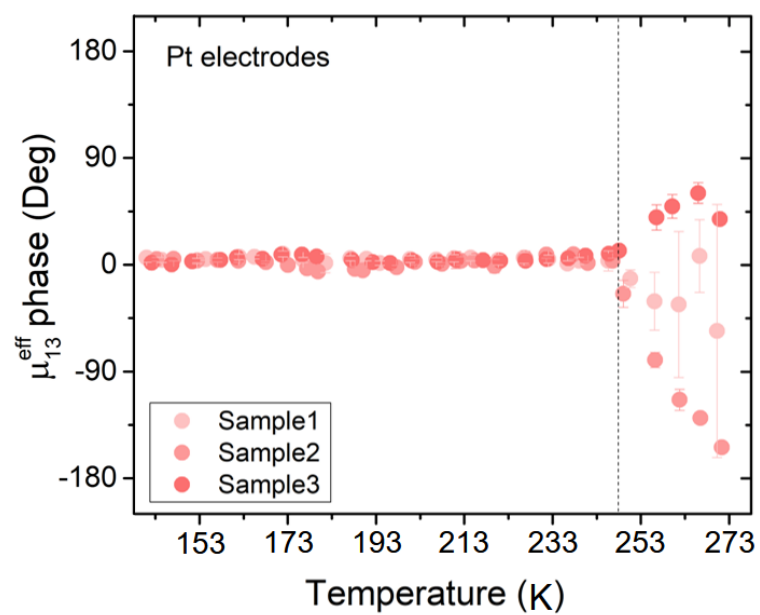


Fig. S8. The phase angle between displacement and charge measured in three ice samples with Pt electrodes on heating. The error bars represent the standard deviation from the average of multiple measurements.

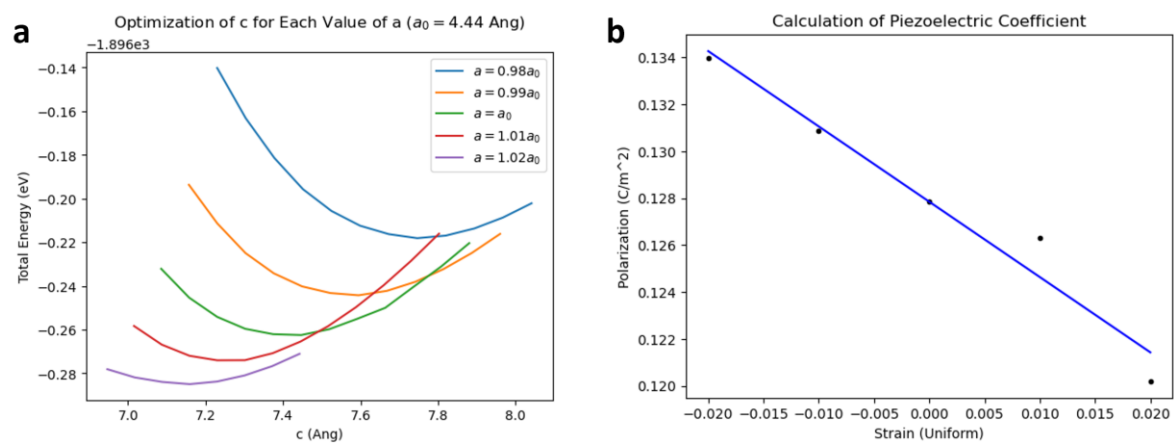


Fig. S9. Calculation of the transverse piezoelectric constant of ice XI.

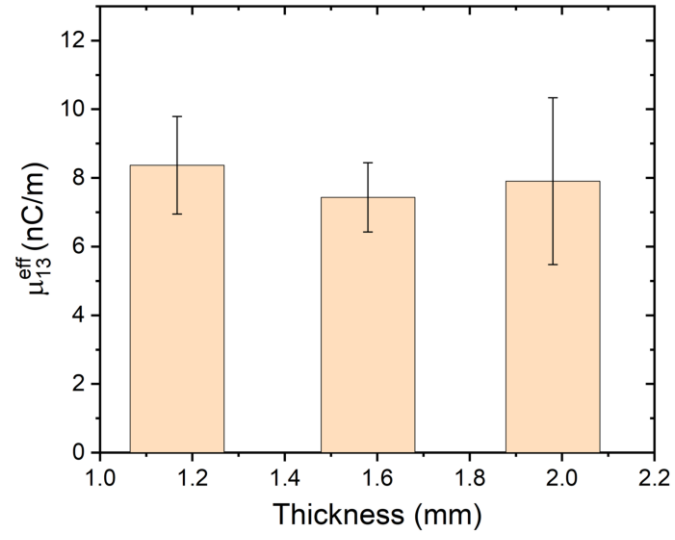


Fig. S10. Thickness dependence of μ_{13}^{eff} for ice with Au electrodes measured at ~160K.

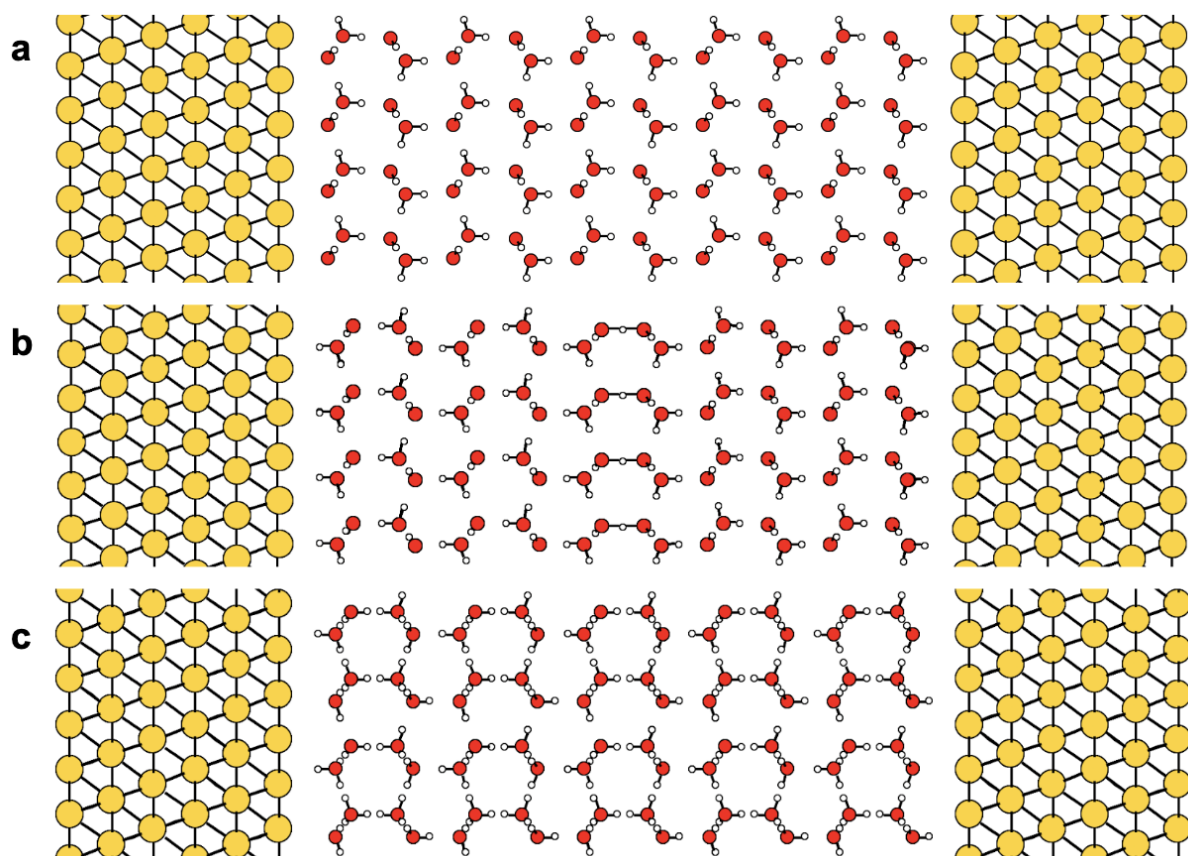


Fig. S11. Illustration of ice XI-Au interface with **(a)** one O-interface and one H-interface, and **(b)** two H-interfaces with a layer of defects in the middle. **(c)** Illustration of ice Ih-Au interface.

$Y=Y_1$ (GPa)	$\nu=\nu_1=\nu_2$	x_r	μ (nC/m)	K_{IC} (kPa m ^{1/2})	σ_a (MPa)
9.33 ²⁷	0.325 ²⁷	100 ²⁷	2.1~8.0 (at 263K)	108.5 ⁵³	0.12 ⁴⁴
w (mm)	l (mm)	$R=R_1$ (μ m)	Y_2 (GPa)	ρ (kg/m ³)	v_r (m/s)
65 ⁴⁴	30 ⁴⁴	10~400 ²⁹	1~9 ^{27,54}	916.7 ²⁷	1~20 ²⁹

Table S1. Parameters used in theoretical calculations.

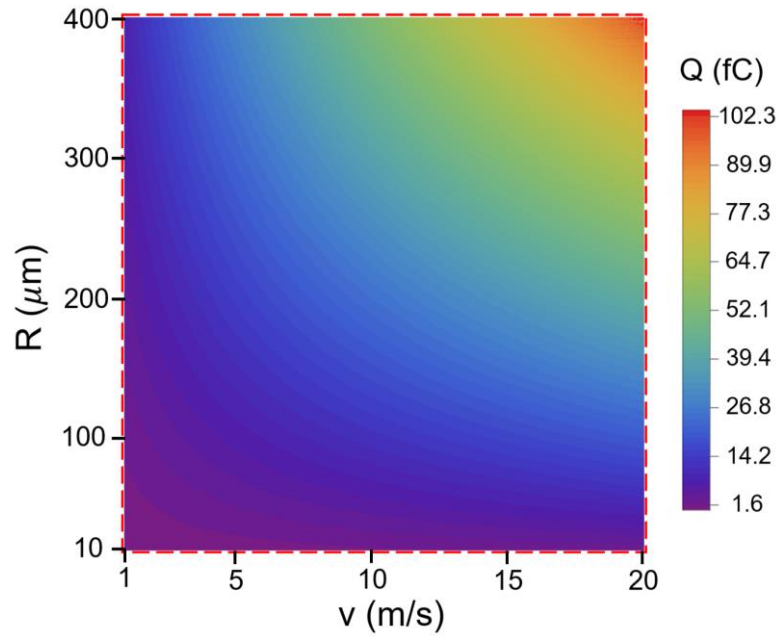


Fig. S12. The size and velocity dependence of surface charge. Parameters: $Y_2=7$ Gpa;
 $\mu_{13}^{eff}=3$ nC/m.

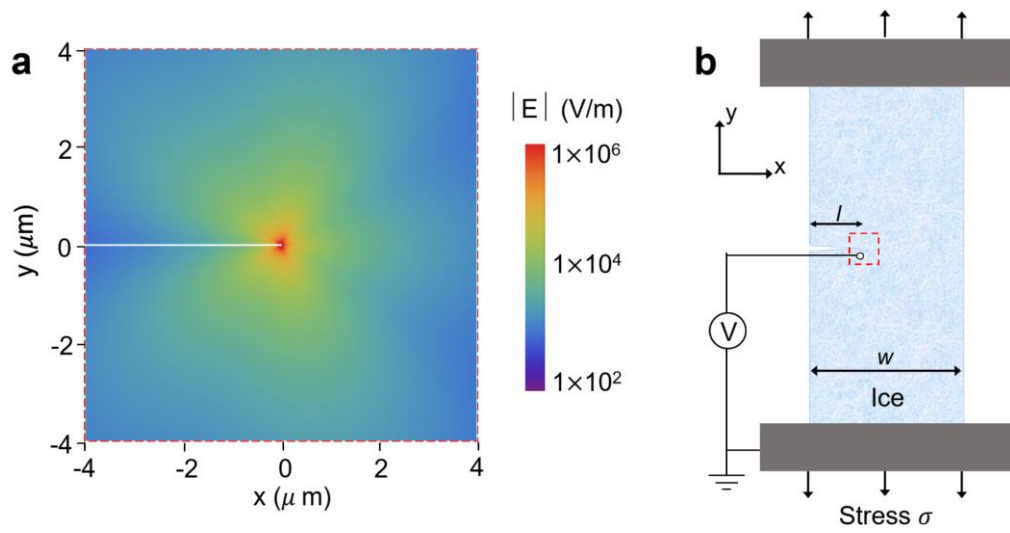


Fig. S13. a, Calculated distribution of the flexoelectric field near a propagating crack apex of ice. **b**, Schematic diagram of the earlier experiment⁴⁴ for measuring the electric potential near a crack apex of an ice specimen under uniaxial tension.

- 1 Bartels-Rausch, T. *et al.* Ice structures, patterns, and processes: A view across the icefields. **84**, 885 (2012).
- 2 Garg, A. High-pressure Raman spectroscopic study of the ice Ih \rightarrow ice IX phase transition. *physica status solidi (a)* **110**, 467-480 (1988).
- 3 Mishima, O., Calvert, L. & Whalley, E. 'Melting ice' at 77 K and 10 kbar: A new method of making amorphous solids. *Nature* **310**, 393-395 (1984).
- 4 Ma, W. & Cross, L. E. Flexoelectricity of barium titanate. *Appl Phys Lett* **88**, 232902, doi:10.1063/1.2211309 (2006).
- 5 Dai, Z., Guo, S., Gong, Y. & Wang, Z. Semiconductor flexoelectricity in graphite-doped SrTiO₃ ceramics. *Ceram Int* **47**, 6535-6539 (2021).
- 6 Zubko, P., Catalan, G., Buckley, A., Welche, P. R. & Scott, J. F. Strain-gradient-induced polarization in SrTiO₃ single crystals. *Phys Rev Lett* **99**, 167601, doi:10.1103/PhysRevLett.99.167601 (2007).
- 7 Narvaez, J., Saremi, S., Hong, J., Stengel, M. & Catalan, G. Large flexoelectric anisotropy in paraelectric barium titanate. *Phys Rev Lett* **115**, 037601, doi:10.1103/PhysRevLett.115.037601 (2015).
- 8 Zubko, P., Catalan, G. & Tagantsev, A. K. Flexoelectric Effect in Solids. *Annual Review of Materials Research* **43**, 387-421, doi:10.1146/annurev-matsci-071312-121634 (2013).
- 9 Tagantsev, A. K. & Yurkov, A. S. Flexoelectric effect in finite samples. *J Appl Phys* **112**, doi:Artn 044103 10.1063/1.4745037 (2012).
- 10 Shu, L. *et al.* Photoflexoelectric effect in halide perovskites. *Nat Mater* **19**, 605-609, doi:10.1038/s41563-020-0659-y (2020).
- 11 Narvaez, J., Vasquez-Sancho, F. & Catalan, G. Enhanced flexoelectric-like response in oxide semiconductors. *Nature* **538**, 219-221, doi:10.1038/nature19761 (2016).
- 12 Pamuk, B., Allen, P. B. & Fernández-Serra, M. V. Electronic and nuclear quantum effects on the ice XI/ice Ih phase transition. *Physical Review B* **92**, doi:10.1103/PhysRevB.92.134105 (2015).
- 13 Ziman, J. M. *Principles of the Theory of Solids*. (Cambridge university press, 1972).
- 14 Pauling, L. The structure and entropy of ice and of other crystals with some randomness of atomic arrangement. *Journal of the American Chemical Society* **57**, 2680-2684 (1935).
- 15 Giauque, W. & Stout, J. The Entropy of Water and the Third Law of Thermodynamics. The Heat Capacity of Ice from 15 to 273° K. *Journal of the American Chemical Society* **58**, 1144-1150 (1936).
- 16 Giauque, W. F. & Ashley, M. F. Molecular rotation in ice at 10 k. free energy of formation and entropy of water. *Physical review* **43**, 81 (1933).
- 17 Zubko, P., Catalan, G. & Tagantsev, A. K. Flexoelectric Effect in Solids. *Annu Rev Mater Sci* **43**, 387-421, doi:10.1146/annurev-matsci-071312-121634 (2013).
- 18 Yudin, P. V. & Tagantsev, A. K. Fundamentals of flexoelectricity in solids. *Nanotechnology* **24**, 432001, doi:10.1088/0957-4484/24/43/432001 (2013).
- 19 Očenášek, J. *et al.* Nanomechanics of flexoelectric switching. *Phys Rev B* **92**, 035417 (2015).
- 20 Wang, B. *et al.* Mechanically induced ferroelectric switching in BaTiO₃ thin films. *Acta Materialia* **193**, 151-162 (2020).
- 21 Lu, H. *et al.* Mechanical writing of ferroelectric polarization. *Science* **336**, 59-61, doi:10.1126/science.1218693 (2012).
- 22 Fischer-Cripps, A. C. *Introduction to contact mechanics*. Vol. 101 (Springer, 2007).
- 23 Park, S. M. *et al.* Flexoelectric control of physical properties by atomic force microscopy. *Appl Phys*

- Rev* **8**, 041327 (2021).
- 24 Mizzi, C. A., Lin, A. Y. W. & Marks, L. D. Does flexoelectricity drive triboelectricity? *Phys Rev Lett* **123**, 116103, doi:10.1103/PhysRevLett.123.116103 (2019).
 - 25 Yang, M. M., Kim, D. J. & Alexe, M. Flexo-photovoltaic effect. *Science* **360**, 904-907, doi:10.1126/science.aan3256 (2018).
 - 26 Saunders, C. J. P. A. E. Charge separation mechanisms in clouds. 335-353 (2008).
 - 27 Petrenko, V. F. & Whitworth, R. W. *Physics of ice*. (OUP Oxford, 1999).
 - 28 Zhang, S.-l., Yang, X.-g. & Zhou, J.-w. A theoretical model for the estimation of maximum impact force from a rockfall based on contact theory. *Journal of Mountain Science* **15**, 430-443 (2018).
 - 29 Takahashi, T. Riming electrification as a charge generation mechanism in thunderstorms. *Journal of Atmospheric Sciences* **35**, 1536-1548 (1978).
 - 30 Gaskell, W. & Illingworth, A. Charge transfer accompanying individual collisions between ice particles and its role in thunderstorm electrification. *Quarterly Journal of the Royal Meteorological Society* **106**, 841-854 (1980).
 - 31 Jayaratne, E., Saunders, C. & Hallett, J. Laboratory studies of the charging of soft-hail during ice crystal interactions. *Quarterly Journal of the Royal Meteorological Society* **109**, 609-630 (1983).
 - 32 Caranti, G., Avila, E. & Ré, M. Charge transfer during individual collisions in ice growing from vapor deposition. *Journal of Geophysical Research: Atmospheres* **96**, 15365-15375 (1991).
 - 33 Avila, E. E. & Caranti, G. M. A laboratory study of static charging by fracture in ice growing by riming. *Journal of Geophysical Research: Atmospheres* **99**, 10611-10620 (1994).
 - 34 Avila, E. E., Varela, G. G. A. & Caranti, G. M. Temperature dependence of static charging in ice growing by riming. *Journal of Atmospheric Sciences* **52**, 4515-4522 (1995).
 - 35 Luque, M. Y., Nollas, F., Pereyra, R. G., Bürgesser, R. E. & Ávila, E. E. Charge separation in collisions between ice crystals and a spherical simulated graupel of centimeter size. *Journal of Geophysical Research: Atmospheres* **125**, e2019JD030941 (2020).
 - 36 Pereyra, R. G. & Avila, E. E. Charge transfer measurements during single ice crystal collisions with a target growing by riming. *Journal of Geophysical Research: Atmospheres* **107**, AAC 23-21-AAC 23-29 (2002).
 - 37 Abdollahi, A. *et al.* Fracture toughening and toughness asymmetry induced by flexoelectricity. *Physical Review B* **92**, doi:10.1103/PhysRevB.92.094101 (2015).
 - 38 Cordero-Edwards, K., Kianirad, H., Canalias, C., Sort, J. & Catalan, G. Flexoelectric Fracture -Ratchet Effect in Ferroelectrics. *Phys Rev Lett* **122**, 135502, doi:10.1103/PhysRevLett.122.135502 (2019).
 - 39 Vasquez-Sancho, F., Abdollahi, A., Damjanovic, D. & Catalan, G. Flexoelectricity in bones. *Adv Mater* **30**, 1705316, doi:10.1002/adma.201705316 (2018).
 - 40 Fifolt, D. A., Petrenko, V. F. & Schulson, E. M. Preliminary study of electromagnetic emissions from cracks in ice. *Philosophical Magazine B* **67**, 289-299, doi:10.1080/13642819308220133 (1993).
 - 41 Thiel, D. V. Electromagnetic emission (EME) from ice crack formation: preliminary observations. *Cold Regions Science and Technology* **21**, 49-60, doi:10.1016/0165-232x(92)90005-f (1992).
 - 42 Fung, Y.-c. A first course in continuum mechanics. *Englewood Cliffs* (1977).
 - 43 Lawn, B. *Fracture of brittle solids*. (Cambridge university press, 1993).
 - 44 Petrenko, V. Electromagnetic emission from cracks in polycrystalline ice. *Abstracts of AGU spring meeting*, 308-309 (1992).
 - 45 Tada, H., Paris, P. C. & Irwin, G. R. The stress analysis of cracks. *Handbook, Del Research Corporation* **34** (1973).

- 46 Shigenari, T. & Abe, K. Vibrational modes of hydrogens in the proton ordered phase XI of ice:
Raman spectra above 400 cm⁻¹. *The Journal of Chemical Physics* **136** (2012).
- 47 Dowell, L. G. & Rinfret, A. P. Low-temperature forms of ice as studied by X-ray diffraction. *Nature*
188, 1144-1148 (1960).
- 48 Bluhm, H., Ogletree, D. F., Fadley, C. S., Hussain, Z. & Salmeron, M. The premelting of ice studied
with photoelectron spectroscopy. *Journal of Physics: Condensed Matter* **14**, L227 (2002).
- 49 Döppenschmidt, A. & Butt, H.-J. Measuring the thickness of the liquid-like layer on ice surfaces
with atomic force microscopy. *Langmuir* **16**, 6709-6714 (2000).
- 50 Golecki, I. & Jaccard, C. Intrinsic surface disorder in ice near the melting point. *Journal of Physics C:
Solid state physics* **11**, 4229 (1978).
- 51 Dosch, H., Lied, A. & Bilgram, J. Glancing-angle X-ray scattering studies of the premelting of ice
surfaces. *Surface science* **327**, 145-164 (1995).
- 52 Sadtchenko, V. & Ewing, G. E. A new approach to the study of interfacial melting of ice: infrared
spectroscopy. *Canadian journal of physics* **81**, 333-341 (2003).
- 53 Nixon, W. & Schulson, E. A micromechanical view of the fracture toughness of ice. *Le Journal de
Physique Colloques* **48**, C1-313-C311-319 (1987).
- 54 Heymsfield, A. J. Cloud Physics. (2003).